Steady state evoked potential (SSEP) responses in the primary and secondary somatosensory cortices of anesthetized cats: nonlinearity characterized by harmonic and intermodulation frequencies

Yota Kawashima[1¶], Rannee Li[1¶], Spencer Chin-Yu Chen[2], Richard Martin Vickery[3], John W. Morley[4], Naotsugu Tsuchiya[1,5,6*]

[1]Turner Institute for Brain and Mental Health, School of Psychological Science, Monash University, Melbourne, Victoria, Australia

[2]Department of Neurosurgery, Robert Wood Johnson Medical School, Rutgers University, New Brunswick, New Jersey, USA

[3]School of Medical Sciences, UNSW Sydney, Sydney, New South Wales, Australia

[4]School of Medicine, Western Sydney University, Penrith, New South Wales, Australia

[5]Center for Information and Neural Networks (CiNet), National Institute of Information and Communications Technology (NICT), Suita, Osaka, Japan

[6]Advanced Telecommunications Research Computational Neuroscience Laboratories, Soraku-gun, Kyoto, Japan

[*]Corresponding author
E-mail: naotsugu.tsuchiya@monash.edu (NT)

[¶]These authors contributed equally to this work.

Abstract

When presented with an oscillatory sensory input at a particular frequency, *F* [Hz], neural systems respond with the corresponding frequency, *f* [Hz], and its multiples. When the input includes two frequencies (*F1* and *F2*) and they are nonlinearly integrated in the system, responses at intermodulation frequencies (i.e., *n1*f1*+*n2*f2* [Hz], where *n1* and *n2* are non-zero integers) emerge. Utilizing these properties, the steady state evoked potential (SSEP) paradigm allows us to characterize linear and nonlinear neural computation performed in cortical neurocircuitry. Here, we analyzed the steady state evoked local field potentials (LFPs) recorded from the primary (S1) and secondary (S2) somatosensory cortex of anesthetized (ketamine-xylazine) cats while we presented slow (*F1*=23Hz) and fast (*F2*=200Hz) somatosensory vibration to the contralateral paw pads and digits. Over 9 experimental sessions, we recorded LFPs from *N*=1620 and *N*=1008 bipolar-referenced sites in S1 and S2 using electrode arrays. Power spectral analyses revealed strong responses at 1) the fundamental (*f1*, *f2*), 2) its harmonic, 3) the intermodulation frequencies, and 4) broadband frequencies (50-150Hz). To compare the computational architecture in S1 and S2, we employed simple computational modeling. Our modeling results necessitate nonlinear computation to explain SSEP in S2 more than S1. Combined with our current analysis of LFPs, our paradigm offers a rare opportunity to constrain the computational architecture of hierarchical organization of S1 and S2 and to reveal how a large-scale SSEP can emerge from local neural population activities.

Introduction

Internal processing architecture of physical systems, including neuronal networks of the brain, can be characterized by probing them with steady oscillatory input at a particular frequency and measuring their output in the frequency domain [1-4]. In sensory neuroscience, this technique is

called a “steady state evoked potential (SSEP)” paradigm. With the oscillatory input probe, the system’s output is examined at various response frequencies. Throughout this paper, we denote input and output frequency with a capital, *F* [Hz], and a small letter, *f* [Hz], respectively. A linear-time-invariant (LTI) system, which does not contain any nonlinearity in the system, can only modulate the amplitude or phase of the responses at $f=F$ [Hz] and cannot generate responses that are not present in the stimulus [4]. The presence of neural response at the harmonics of the input frequency ($n*f$, where n=2, 3, 4, …) necessitates nonlinear processing in the system. Recently, the SSEP paradigm and its variants have arisen as a powerful technique in sensory neuroscience to characterize properties of the sensory neural circuits in the visual, auditory and somatosensory systems in various animal species [3-8].

The SSEP paradigm is particularly powerful when extended to use multiple input frequencies. For the case of two input frequencies ($F1$, $F2$), as used in this paper, in addition to the harmonic frequencies, nonlinear processing in the system can be further inferred by the presence of intermodulation frequencies ($n1*f1+n2*f2$) in the output of the system [1, 2, 6, 9-14] (See a review [15]). Intermodulation responses can only arise from nonlinear processing of two (or more) input frequencies, e.g., $F1$ and $F2$. Recent cognitive neuroscience investigations have utilized this theoretical prediction [4-6, 11-13]. While these intermodulation phenomena are attracting popularity in large scale EEG measures in human cognitive neurosciences, the detailed neuronal mechanisms on how intermodulation arises at the level of single neurons and local neural circuitry remains unclear.

Previously, we applied the SSEP paradigm in the somatosensory domain in the anesthetized cats [16], focusing on the analysis of isolated single (or multiple) neuron spiking activities. There, we observed neurons responding in synchrony with the low frequency stimulus ($F1$=23Hz), and neurons that seemed partially time-locked to the high frequency input

(*F2*=200Hz) (data not published). Further we found some neurons that responded to low (*F1*=23Hz) and high (*F2*=200Hz) frequency vibrations in a manner where the spiking rates were linearly related to the amplitude of the respective vibratory inputs. We also found that some neurons responded to these vibratory inputs in a supralinear facilitatory manner.

In this paper, we turned our analysis to local field potentials (LFPs) recorded in the same experiments in order to examine the population-level neuronal responses at the harmonic and intermodulation frequencies of the input stimuli. While a single cortical neuron may not be able to respond to every cycle of the very high frequency stimulus (e.g., *F2*=200Hz) due to the refractory period, neurons are capable of collectively encoding every cycle at such a high frequency. As LFPs reflect collective actions of neurons, we examine LFPs for high frequency neural population response and evidence of nonlinear processing that manifests as responses at harmonic (2*f1*, 3*f1*, etc) and intermodulation (*n1*f1*+*n2*f2*) frequencies.

We found that LFPs recorded in the primary and secondary somatosensory cortices of anesthetized cats indeed show strong evidence of nonlinear processing from the examination of the SSEP harmonic and intermodulation. Unexpectedly, we also found that non-harmonic and non-intermodulation frequencies between 50-150Hz in the secondary somatosensory cortex can be strongly modulated by the strength of the vibratory inputs. Finally, our computational modeling suggests that nonlinear processing is prominent in the secondary somatosensory cortex, but less so in the primary sensory cortex. Our results constrain the network architecture of the somatosensory cortical circuits. It will inform future studies that aim to generalize our findings to other sensory modalities, animal models, and conscious states.

Methods

Experimental subjects and procedures

The detailed experimental methods are described in [16]. Here we describe the aspects of the protocol that are relevant for our current paper. This study was carried out in strict accordance with the recommendations in the Guide for the Care and Use of Laboratory Animals of the National Health and Medical Research Council, Australia. All procedures involving animals were approved and monitored by the University of New South Wales Animal Care and Ethics Committee (project number: ACEC 09/7B). All surgery was performed under ketamine-xylazine anesthesia, and all efforts were made to minimize suffering.

Outbred domestic cats had anesthesia induced with an intramuscular dose of ketamine (20 mg/kg) and xylazine (2.0 mg/kg). Anesthesia was maintained over the three days of an experiment by intravenous infusion of alfaxalone (1.2 mg/kg) delivered in an equal mixture of Hartmann's solution and 5% glucose solution at approximately 2 ml/kg/hr. The animal received daily doses of dexamethasone (1.5 mg/kg) and a broad spectrum antibiotic (Baytril, 0.1 ml/kg) intramuscularly, and atropine (0.2 mg/kg) subcutaneously.

The animal was secured in a stereotaxic frame and a craniotomy and durotomy were performed to expose the primary and secondary somatosensory areas (Fig 1A). The exposed cortex was mapped by recording evoked potentials using a multichannel recording system (RZ2 TDT, Tucker Davis Technologies Inc., Florida, U.S.A) and an amplifier and headstage (model 1800, AMSystems, Washington, U.S.A.).

----- Fig 1 around here -----

140

141 We used the RZ2 TDT system to drive a Gearing & Watson mechanical stimulator with a 5mm
142 diameter flat perspex tip. As vibrotactile stimuli, we delivered *F1*=23Hz or *F2*=200Hz sinusoidal
143 indentation to the paw pad or digit of the cat. The peak-to-peak amplitude of the sinusoid for
144 23Hz ranged from 0 to 159μm, while that for 200Hz ranged from 0 to 31μm. The probe at rest
145 barely indented the skin. Hair around the forelimb paw pads was shaved to prevent activation
146 during stimulation.

147

148 We recorded neural activity with a 10x10 ‘‘planar’’ multi-electrode array (Blackrock
149 Microsystems, Utah, U.S.A) in S1 and with a 8x8 ‘‘linear’’ multi-electrode array (NeuroNexus,
150 Michigan, U.S.A.) in S2. We inserted these arrays aiming at recording from the paw
151 representation regions within S1 and S2. Through the mapping procedure, we confirmed these
152 recording sites. We used the planar arrays to obtain wide coverage of S1 and nearby regions.
153 The array consisted of 1.5mm long electrodes and recorded data from those electrodes across
154 a 13mm^2 horizontal plane of cortex. We chose to use the linear array to record neural activity
155 from S2 because S2 is buried in the depth of the cortex. The electrode contacts on the linear
156 array recorded data from a vertical cross-section of multiple cortical layers along 1.4mm of
157 cortex. Data from these arrays were collected using the RZ2 TDT multichannel recording
158 system through a PZ2 TDT pre-amplifier. Streaming data were recorded simultaneously without
159 filtering at 12kHz.

160

161 Stimulus duration varied across sessions (Table 1), ranging from 3 to 4.4s. The peak-to-peak
162 amplitude of the low frequency sinusoid varied from 0 and 159μm, and the high frequency
163 sinusoid from 0 to 31μm. The amplitudes for the two sinusoids were selected pseudorandomly
164 for each trial within each session. The number of trials per stimulus condition (a particular
165 combination of *F1* and *F2* amplitude) ranged from 10-15 depending on the recording session.

166

167 **Table 1. Summary of the experiments.**

Session ID	Location of vibratory stimulation	23Hz stimulus amplitudes [μm]	200Hz stimulus amplitudes [μm]	# of trials per condition	Stimulus duration [s]
1-1	Contralateral D5	0, 10, 20, 40, 79, 159	0, 1, 2, 4, 7, 15	10	4
1-2	Contralateral D4	0, 10, 20, 40, 79, 159	0, 1, 2, 4, 7, 15	10	4
1-3	Contralateral D5	0, 19, 40, 79, 159	0, 2, 4, 7, 15	15	4
2-1	Contralateral D4	0, 40, 79, 159	0, 4, 7, 16	15	3
2-2	Contralateral D5	0, 40, 79, 159	0, 4, 7, 16	15	3
2-3	Contralateral central pad	0, 40, 79, 159	0, 4, 7, 16	15	3
2-4	Contralateral central pad	0, 19, 40, 79, 159	0, 4, 7, 16, 31	10	4.4
2-5	Contralateral central pad	0, 19, 40, 79, 159	0, 4, 7, 16, 31	10	4.4
2-6	Contralateral D4	0, 19, 40, 79, 159	0, 4, 7, 16, 31	10	4.4

168 The details of the stimulus configuration per session. Each row has a distinct session ID. The
169 first digit of the session ID refers to the cat ID. Within the same cat, we did not move S1
170 recording locations, but in some cases, we moved S2 recording locations. The second digit
171 refers to different vibratory stimulation locations (e.g., pad, Dx finger, etc). We recorded from 2
172 cats over 9 sessions. 0 stimulus amplitude means no vibration at that frequency.

173

Data preprocessing

To reduce line noise and obtain finer spatial resolution, we first applied bipolar re-referencing to the original LFP data, by subtracting the unipolar referenced voltage of each electrode from the horizontal or vertical neighbouring electrode [17]. Throughout this paper, we call the resulting bipolar re-referenced data as “bipolar channels”. Bipolar re-referencing resulted in 180 bipolar channels (90 vertical and 90 horizontal pairs) for 10x10 planar array recordings and 112 bipolar channels (56 vertical and 56 horizontal pairs) for 8x8 linear array recordings (in total 2628 channels over 9 sessions).

For all subsequent analyses, we epoched each trial data into a single 2s segment (from 0.5 to 2.5s after stimulus onset), which excludes initial transient responses. 2s is long enough for our analyses and is consistently available across all sessions. We excluded the datasets where we used 0.8s as a stimulus duration (and *F1*=20Hz) which was mainly reported in [16]. All the experiments we report here come from experiments with *F1*=23Hz and *F2*=200Hz.

Analysing power

By $\log P^{i,t,[g,h]}(f)$, we denote the logarithm (base 10) of power at frequency, f, of the LFP over 2s for channel i in trial t, where the amplitude of *F1*=23Hz and *F2*=200Hz was g and h [μm]. Hereafter, we simply call “power” to mean “logPower” for all subsequent analysis and statistics. We analyze the response frequency f from 0 to 250Hz. To obtain $\log P^{i,t,[g,h]}(f)$, we used *mtspectrumc.m* from Chronux Toolbox [18 Oxford University Press] with one taper. Together with the 2s time window length, this gives a half bandwidth of 0.5Hz ($=(k+1)/2T$; here, k is the number of tapers and T is the length of time window). The mean logPower $\underline{\log P^{i,[g,h]}}(f)$ is the mean across all trials in each stimulus condition. We use $\underline{X}$ to denote mean of X across trials.

We had several channels whose power happened to be 0 in some trials in some frequencies, which resulted in negative infinity after log transform. We removed these channels from further analysis.

We define signal to noise ratio (log*SNR*) of the response, $\log SNR^{i,t,[g,h]}(f)$, by subtracting the logPower at the neighbouring frequencies of *f* [Hz](denoted by a set *F'* with $F' = \{f' \mid f-3<f'<f-1 \text{ or } f+1<f'<f+3\}$) from the logPower at *f*;

$$\log SNR^{i,t,[g,h]}(f) = \log P^{i,t,[g,h]}(f) - \frac{1}{N_{F'}} \sum_{f' \in F'} \log P^{i,t,[g,h]}(f') \quad (1)$$

, where $N_{F'}$ is the number of the neighbouring frequencies. log*SNR* is a standard measure in SSEP literature [4] and facilitates comparisons of the signal quality across different recording modalities, brain regions, animals and paradigms. As our input stimulus contained sinusoidal tactile modulation at *F1*=23Hz and *F2*=200Hz, we expected that there would be log*SNR* in the corresponding tagged frequencies *f1*=23Hz and *f2*=200Hz. Further, we expected that nonlinear processing to result in log*SNR* in the harmonic frequencies (i.e., the integer multiple of the tagged frequencies, *n1*f1*). As we restricted our analyses within 0 to 250Hz, we analyzed 9 harmonic frequencies: 46, 69, 92, 115, 138, 161, 184, 207, and 230Hz with *n1*=2, 3, 4, 5, 6, 7, 8, 9 and 10, respectively. We further expected that nonlinear integration of the two stimuli to result in log*SNR* at the intermodulation frequencies, *n1*f1+n2*f2*, where *n1* and *n2* are both nonzero integers. When *n2*=1, this resulted in 10 intermodulation frequencies: 16, 39, 62, 85, 108, 131, 154, 177, 223, and 246Hz, with *n1*=-8, -7, -6, -5, -4, -3, -2, -1, 1, and 2, respectively. In total, we considered 21 frequencies (2 tagged, 9 harmonic, and 10 intermodulation frequencies). Note that the closest neighboring frequencies among tagged, harmonic, and

intermodulation frequencies are 7Hz (e.g., *f1*=23Hz vs (-8)**f1*+*f2*=16Hz), which is much bigger than the half bandwidth of 0.5Hz (see above).

Here, log*SNR* assumes that frequencies outside of tagged, harmonic, and intermodulation frequencies reflect the noise and do not reflect the processing of the stimuli [4]. We were, at least initially, agnostic about such an assumption (See Discussion on this issue).

We also define vibration evoked logPower, $VELogP^{i,t,[g,h]}(f)$, as logPower minus mean logPower across trials in which the stimulus probe touched the cat's paw without any vibration (i.e. [*g*, *h*]=[0, 0]). That is,

$$VELogP^{i,t,[g,h]}(f) = \log P^{i,t,[g,h]}(f) - \frac{1}{N_T}\sum_{t' \in T} \log P^{i,t',[0,0]}(f) \qquad (2)$$

, where *T* is a set of [*g, h*]=[0, 0] trials and N_T is the number of such trials. Like log*SNR*, we expected that there would be *VELogP* in the target, harmonic, and intermodulation frequencies.

In addition to the tagged, harmonic, and intermodulation frequencies, we observed broad high-gamma responses [19-22]. In our preliminary analyses, where we examined the responses of all frequencies that are outside of the tagged, harmonic, and intermodulation frequencies, we observed strong modulation of the high-gamma band (50-150Hz) power with some dependency on the amplitude of *F1* and *F2* vibration. If there is a strong evoked broadband response, the log*SNR* measure would not detect such an increase. Broad and uniform increase of power will cancel out due to the neighborhood-subtraction procedure in logPower, resulting in log*SNR*(*f*)=0. To analyze the observed high-gamma responses, we used a different measure, high gamma power (HGP), in which we selectively averaged the power in the high gamma

range excluding any contribution from tagged, harmonic and intermodulation frequencies. For this purpose, we first define a set of frequencies, *f'*, between 50 and 150Hz, which are outside of +/- 0.5Hz around the tagged, harmonic, and intermodulation frequencies. We define high gamma power (log*HGP*) as the mean vibration evoked logPower (*VELogP*) across *f'* as follows:

$$\log HGP^{i,t,[g,h]} = \frac{1}{N_{f'}} \sum_{50<f'<150} VELogP^{i,t,[g,h]}(f') \tag{3}$$

,where $N_{f'}$ is the number of the frequencies considered for HGP.

Statistical analysis

To investigate the effect of the amplitude of vibration stimuli at *F1* and *F2*, we performed a two-way analysis of variance (ANOVA) using the MATLAB function, *anova2.m* (MATLAB R2019b). We modelled the dependent variable *y*, where *y* can be log*P*(*f*), log*SNR*(*f*), or *VELogP*(*f*), at channel *i*, and response frequency *f*:

$$y(i,f) = cF_1 \times aF_1 + cF_2 \times aF_2 + cF_1F_2 \times aF_1 \times aF_2 + \varepsilon \tag{4}$$

, where *aF1* and *aF2* are the amplitude of *F1*=23Hz and *F2*=200Hz vibration stimuli (e.g., [*aF1*, *aF2*]=[0, 0], [0, 40].... See Table 1) and *cF1*, *cF2*, *cF1F2* are the coefficient that minimizes the error term, *ε*, in the ANOVA framework. We performed the ANOVA to obtain *F*-statistics and *p*-value separately for each channel, *i,* and response frequency, *f,* for two main effects and their interaction, by testing the significant departure of *cF1*, *cF2* and *cF1F2* from zero.

We performed the above ANOVA for frequencies from 0Hz to 250Hz for each channel. To correct for multiple comparisons, we used false discovery rate [23] implemented as *fdr.m* in eeglab for MATLAB [24]. We set the false discovery rate as q=0.05 to determine a corrected p-value threshold for significance by pooling across all frequencies, bipolar channels, sessions, somatosensory areas, and three effects (two main effects and their interaction).

Results

Steady state evoked potentials (SSEP) at a channel in the maximal stimulation condition

We used the steady state evoked potentials (SSEP) paradigm to probe the properties of population-level neuronal responses in cat's primary and secondary somatosensory areas (S1 and S2) under anesthesia. While we recorded local field potentials (LFPs) from planar array in S1 and linear electrode array in S2 (Fig 1A), we applied vibratory stimuli in low ($F1$=23Hz) and high ($F2$=200Hz) frequency around the cats' paw (Fig 1B and Table 1). In Fig 1C, we show a sample LEP response from one highly responding bipolar channel in S1 in Session 2-2. In the figure, we show the average of the bipolar data across 15 trials in which we applied the largest amplitude in the session, that is, stimulus condition [$F1$, $F2$] = [159,16]. Hereafter, we represent a combination of the vibration amplitude X and Y [μm] for frequency $F1$ and $F2$ as [$F1$, $F2$]=[X, Y].

To characterize neural responses at tagged, harmonic and intermodulation frequencies, we first computed the power spectra from 0 to 250Hz for each trial in each stimulus condition (see Methods) in total from 2628 channels. Fig 1D shows the power spectrum from the same

293 channel in S1 as in Fig 1C (the average across 15 trials from the maximum stimulus condition,
294 [*F1*, *F2*] = [159, 16], in Session 2-2). The frequencies of interest are shown: *f1*=23Hz
295 fundamental and harmonic frequencies with red vertical line, *f2*=200Hz fundamental frequency
296 with green vertical line and their intermodulations with blue vertical line. In the figure, we
297 observe several peaks, but 1/*f* distribution is dominant. To isolate the significance of responses
298 at the frequencies of interest, we quantified the power increase from the baseline. First,
299 following the SSEP literature [4], we used nontagged frequencies as the baseline. We refer to
300 the measurement as signal to noise ratio (log*SNR*). Second, we used the no-stimulus condition,
301 i.e. [*g*, *h*]=[0, 0], as the baseline. We refer to the measurement as vibration evoked logPower
302 (*VELogP*; see Methods for the details). log*SNR* and *VELogP* were computed per trial, stimulus
303 condition, and channel. Figs 1E and 1F show the example of log*SNR* and *VELogP* from the
304 same channel as in Figs 1C and 1D (the average across 15 trials at [*F1*, *F2*] = [159, 16] in
305 Session 2-2). These formats clarify the peaks of log*SNR* and *VELogP* at the frequencies of
306 interest. As we will demonstrate, these observations were not unique to one particular channel,
307 but generalized across many channels. Note that these results were not straightforwardly
308 expected from our previous study with SUA and MUA in the same data set [16]. We will discuss
309 the implication of each point in Discussion.

310

311 Unexpected main effects and interactions of *F1* and *F2* 312 across frequencies

313 Next, we quantified the response dependency on the magnitude of *F1*, *F2* and their interactions
314 by performing two-way ANOVA on log*P*, log*SNR* and *VELogP*. The statistical analyses revealed
315 spatially specific responses for the frequencies of interest (Fig 2). For example, we found that
316 some channels responded at *f1* (or *f2*), whose response magnitude depended on only the

stimulus magnitude of *F1* (or *F2*) (Figs 3 and 4). However, we also found that some channels responded at *f1* (or *f2*), whose response magnitude depended on the stimulus magnitude of the "other" frequency, e.g., *F2* (or *F1*) (Fig 5). Further, we found that the assumption of log*SNR* computation, that is, the use of nontagged frequencies as the baseline was violated in some notable cases. This is hinted at by the difference between log*SNR* and *VELogP* around 50<*f*<150Hz in Fig 2B (black line). As we elaborate in Fig 6, we found this effect only in the channels in S2 and at 50<*f*<150Hz, so-called high gamma range.

Three major response types observed

Using two-way ANOVA, we statistically evaluated the proportion of the 2628 channels that exhibited significant modulation in log*P*, log*SNR*, and *VELogP*. The factors were the input amplitude of *F1*=23Hz and *F2*=200Hz vibration. This analysis revealed that response at a frequency was mainly classified into three types: 1) response modulated by only *F1* amplitude (Fig 2A), 2) one modulated by only *F2* amplitude (Fig 2B), and 3) one modulated by the two amplitude and their interaction (Fig 2C). In addition, we found that the results from log*SNR* were different from those from log*P* and *VELogP*. In particular, while we observed modulation at 50Hz<*f*<150Hz in log*P* and *VELogP*, this modulation was not observed in log*SNR*. When it comes to *VELogP*, the results were exactly the same as ones of log*P* because of our definition of *VELogP*.

Figs 2A-2C respectively show the percentages of channels showing type 1), 2) and 3) significance for log*P*, log*SNR* and *VELogP* at each frequency. The frequencies of interest are shown with red (23Hz fundamental and harmonic frequencies), green (200Hz), and blue (intermodulation frequencies). The first type of response (Fig 2A) is found predominantly at the integer multiples of *f1*=23Hz (~4%) and some intermodulation frequencies (~1%). Unlike the first

342 type, the second type (Fig 2B) is mainly found at *f2*=200Hz (~12%). Interestingly, this type is
343 also found at 50<*f*<150Hz (~2% on average), so-called high gamma range. Finally, the third
344 type (Fig 2C) is predominantly found at *f1*=23Hz (~6%) and 2*f2*=46Hz (~7%), but also observed
345 across some harmonic and intermodulation frequencies as well as *f2*=200Hz (~2%).
346
347 ----- Fig 2 around here -----
348
349 In the next few sections, we will show exemplar log*SNR* responses of the three response types
350 from Session 2-2. (See Sup Figs 1-3 for exemplar *VELogP* responses.)
351

352 Exemplar responses at *f1* (=23Hz) only dependent on the
353 magnitude of *F1* (=23Hz)

354 In Fig 3, we show exemplar responses at *f1*=23Hz which are modulated by only the magnitude
355 of stimulus vibration at *F1*=23Hz. Fig 3A depicts log*SNR* around 23Hz at bipolar channel 131 in
356 S1 in Session 2-2. The channel demonstrates a significant main effect of *F1*=23Hz amplitude
357 ($p<10^{-5}$), but neither the main effect *F2*=200Hz (p=0.054) nor their interaction (p=0.52; the
358 corrected threshold 0.00019). Fig 3A shows that log*SNR* at 23Hz was significantly modulated as
359 a function of *F1*=23Hz amplitude from 0 to 159μm (from the top to the bottom row) but not
360 across the amplitude of *F2*=200Hz amplitude from 0 to 16μm (from the left to the right column).
361 Fig 3B shows the spatial distribution of log*SNR* for all channels in S1 during Session 2-2. We
362 use a blue diamond to mark the channel shown in Fig 3A.
363
364 ----- Fig 3 around here -----
365

Exemplar responses at *f2* (=200Hz) only dependent on the magnitude of *F2* (=200Hz)

Fig 4 shows exemplar responses at *f2*=200Hz which are modulated by only the magnitude of stimulus vibration at *F2*=200Hz. Fig 4A depicts log*SNR* around 200Hz for bipolar channel 36 in S1 in Session 2-2. The channel demonstrates a significant main effect of *F2*=200Hz amplitude ($p<10^{-5}$), but not the interaction (p=0.14). The main effect of *F1*=23Hz (p=0.00043) does not survive the correction for multiple comparisons (0.00019). Fig 4B shows the spatial distribution of log*SNR* for all channels in S1 during Session 2-2. It is clear that while many channels increase their log*SNR* as the amplitude of 200Hz increases (from the left to the right column), a cluster of channels above bipolar channel 36 (blue diamond) also increases log*SNR* at 200Hz as the amplitude of 23Hz increases (from the top to the bottom row).

----- Fig 4 around here -----

Exemplar responses at *f1* dependent on the magnitude of *F1* and *F2* and their interaction

Fig 5 shows exemplar responses at *f1*=23Hz which are modulated by magnitude of stimulus vibration at both *F1* and *F2* and their interaction. Fig 5A depicts log*SNR* around *f*=23Hz for bipolar channel 158 in S1 in Session 2-2. The channel demonstrates the significant main effects of both 23Hz ($p<10^{-5}$), 200Hz ($p<10^{-5}$) as well as interaction ($p<10^{-5}$) with the corrected threshold 0.00019. Fig 5B shows the spatial distribution of log*SNR* for all channels in S1.

----- Fig 5 around here -----

Violation of SNR computation in the high gamma band in S2, but not in S1.

The steady state evoked potentials (SSEP) paradigm assumes that the responses at the "nontagged" frequencies (i.e., outside of the tagged, harmonic and intermodulation frequencies) do not represent stimulus processing, thus, it can be considered as the noise or baseline. The log*SNR* measure we presented so far rests on this assumption. To contrast the difference between log*SNR* and *VELogP* responses, we present the data in Figs 3-5 in the format of *VELogP* in Sup Figs 1-3.

Figs 6A-6C show the *F*-statistics for *F1* main effect, *F2* main effect, and their interaction respectively from our two-way ANOVA on *VELogP* (not log*SNR*) across all frequencies from 0 to 250Hz. Each of them shows the 95th, 90th, and 50th percentile for *F*-statistics for *N*=1620 channels in S1 and *N*=1008 channels for S2. For these figures, we removed +/-0.5Hz around the fundamental, harmonic and intermodulation frequencies in order to focus on the modulation of responses at the nontagged frequencies. Blue and pale blue lines for S1 in Figs 6A-6C demonstrate that S1 does not show any effects outside the fundamental, harmonic, and intermodulation frequencies. Red and pale red lines for S2 are very similar in Figs 6A and 6C. However, they are quite distinct in Fig 6B, which demonstrates a strong main effect of *F2*=200Hz across HGB (from 50 to 150Hz) in some channels in S2. Fig 7A shows one exemplar response in bipolar channel 102 from Session 2-2 in S2, which shows clear main effects of *F2*=200Hz across 50-150Hz. Fig 7B shows the spatial mapping of HGP in S2, which demonstrates the wide spread high gamma responses in S2. (See Methods for HGP.)

----- Fig 6 around here -----

----- Fig 7 around here -----

The result is quite unlike all the analyses we presented so far, where we see no clear differences between the two regions, S1 and S2. We will come back to the source of the differences and its implication in SSEP paradigm in Discussion.

HGP is sustained after the onset transient

HGP is typically observed as a transient response [22, 25], thus, the fact that we saw the HGP may be dependent on our choice of the duration of the response for computing the spectral power. To examine this, we analyzed the time course of the HGP. Here, we shortened the time window from 2 to 0.5s, thus, the half bandwidth increased from 0.5 to 2Hz. To avoid the influence of the tagged frequencies, we averaged the power from 50 to 150Hz except for 2Hz around the tagged frequencies.

Based on the ANOVAs results, we searched for channels where HGP was modulated by the amplitude of *F2* stimulus vibration. Specifically, we used *F*-stats results from ANOVAs performed on log*P*. We took the mean of the *F*-stats across frequencies from 50 to 150Hz, avoiding the frequencies of interest +-2Hz for each channel and selected the top 10% of channels that showed larger mean *F*-stats.

Fig 8 shows the mean time course of HGP (black line) and responses at frequencies of interest around HGB from the top 10% channels. When computing the mean time course, we took only the maximum stimulus condition from each session. The HGP increase was prominent at the stimulus onset of the transient. After the transient, however, the HGP persisted and its magnitude was sometimes as strong as responses at harmonic and intermodulation frequencies. This sustained increase of HGP in nontagged frequencies violates the assumption

for the computation of signal-to-ratios; that is, nontagged frequencies do not reflect the stimulus processing and can serve as the baseline for the computation of log*SNR*. We will return to this issue in Discussion.

----- Fig 8 around here -----

Computational models to account for the observed nonlinear processing

As have been demonstrated so far, in addition to the targeted stimulus frequencies, *f1*=23Hz and *f2*=200Hz, we observed strong response modulation at the harmonic and intermodulation frequencies as a function of the vibration amplitude of *F1* and *F2* stimuli (Figs 1 and 2). Harmonic and intermodulation responses, especially the latter, have been taken as evidence of nonlinear processing in brains [15]. How such nonlinear processing is achieved by the neural circuitry in the brain, however, remains unclear.

In order to infer potential neural mechanisms which could give rise to the observed nonlinear responses, we used a computational modelling approach. Given the demonstrated biological plausibility [15, 26, 27], here we focused on two types of nonlinear processing, that is, rectification and square wave. For a sinusoidal input $X=\sin(2\pi * f * t)$, where t is time and f is input frequency, we modelled rectification nonlinearity as,

$$Rect(X) = \begin{cases} X & (\text{if } X > 0) \\ 0 & (\text{otherwise}) \end{cases} \tag{5}$$

, and square-wave nonlinearity as,

$$Sq(X) = \begin{cases} 1 & (\text{if } X > 0) \\ -1 & (\text{otherwise}) \end{cases} \tag{6}$$

Using an information theoretic model comparison approach, we selected the most plausible model among candidates, separately for those observed within S1 and S2.

As is reviewed by Gordon et al. 2019, these nonlinear operations, *Rect(X)* and *Sq(X)*, alone do not generate responses at harmonic nor intermodulation frequencies (Fig 9) while they do so when combined with further operations, such as multiplication. To reduce possible model architectures, we first visually inspected the data and the outputs from canonical models (Fig 9). We considered two classes of models; one based on combinations of *Rect* and the other based on *Sq*. For the *Rect* class, we considered *Rect(X)+Rect(Y)+Rect(XY)+Rect(X)Rect(Y)* as a full model and compared its reduced model by model comparison procedure using Akaike's Information Criteria (*AIC*) [28]. For the *Sq* class, we considered *Sq(X)+Sq(Y)+Sq(XY)* as the full model (*Sq(X)Sq(Y)* is analytically identical to *Sq(XY)* when *X* and *Y* are real numbers). Fig 9 displays waveforms in the time-domain and spectra in the frequency-domain for each model class with coefficients set to be 1 for all terms.

----- Fig 9 around here -----

In the fitting step, we used a simple line search optimization technique [29] to optimize coefficients for each term (for the details, see Sup Appendix 1). This optimization minimized the difference between the log*SNR* of the model output and the observed mean log*SNR* for a given channel across the frequencies of interest (Fig 10B). We adopted the mean log*SNR* across

trials from the maximum vibration condition. For a given channel, we thus have 6 sets (4 for rectification and 2 for square wave class) of the best fit coefficients and the minimum difference between model and actual log*SNR*.

To focus on a possible neuronal mechanism of harmonic and intermodulation nonlinear responses, we focused on the real channels that showed these nonlinear responses strongly. Specifically, we chose the top 10% channels for S1 (156 out of 1620 channels) and S2 (101 out of 1008 channels) in terms of the sum of log*SNR* across harmonic and intermodulation frequencies at the maximum stimulus condition.

Fig 10 illustrates exemplar model responses. Fig 10A shows log*SNR* for the real data (bipolar channel 43 in S1 in Session 2-2) and the optimized models while Fig 10B shows the difference between the real data and the optimized model at the frequencies of interest, that is, *f1*, *f2* fundamentals, harmonic, and intermodulation frequencies. For this channel, we see that log*SNR* at intermodulation frequencies at 177Hz and 223Hz are completely missed by the simplest model (i.e., *Rect(X)+Rect(Y)*), while they are explained by the rest of three non-linear models. However, *Rect(XY)* nonlinearity cannot account for log*SNR* at 154Hz and 246Hz. *Rect(X)Rect(Y)* is required to explain these components. We observed only slight improvement by the full model (i.e. *Rect(X)Rect(Y)* and *Rect(XY)*). Unlike *Rect* nonlinearity, we found *Sq* nonlinearity to perform rather poorly for both tagged and nontagged frequencies (Sup Fig 4).

----- Fig 10 around here -----

Fig 11 summarizes the population level statistics of the model fitting, which shows obviously better results with rectification models (median minimum differences are 50-70) over square wave models (median minimum differences are around 90-110 in Sup Fig 5).

To address the question of whether integrative computation is observed more frequently in S2 than S1, we compared the model fitting results between S1 and S2. Cumulative probability distributions in Fig 11A demonstrates that the simplest *Rect(X)+Rect(Y)* model, depicted by the blue lines, captures most of the variance for S1 responses while it fails to do so for S2. Adding another integrative nonlinear *Rect(XY)* component (orange lines) nearly saturated our model performance for S1, while it still left room for improvement for S2. Additional improvement was achieved when we considered *Rect(X)Rect(Y)* component (purple and yellow), which led to an improvement only in S2.

To take into account the number of parameters used for each model class, we computed Akaike's Information Criterion (*AIC*) [28] for each model class within S1 and S2 (See Sup Appendix 2 for the details). Fig 12 shows *AIC* for 6 models, demonstrating the fitting performance is best for the full rectification model for both S1 and S2, even when we corrected for the bias due to the increased number of model parameters.

Finally, we confirmed the statistical difference of the cumulative probability distributions between S1 and S2 for each model. Kolmogorov-Smironv tests confirmed a significantly better model fit ($p<10^{-5}$) for S1 than S2 for the simplest model (Fig 11B top left). Although the three components models resulted in better performance for S1 than S2, the difference was not as large as the simplest model (p=0.0039 for the model with *Rect(XY)* in Fig 11B top right and p=0.019 for the model with *Rect(X)Rect(Y)* in Fig 11B bottom left). For the full model, the difference in model fitting was not significant (p=0.054 in Fig 11B bottom right). (All p values were Bonferroni corrected). These results suggest that the integrative nonlinear components played a significant role in explaining the variance of S2 channels to make the quality of our model fitting equivalent

between S1 and S2.These analyses confirm the presence of more complex integrative nonlinear interactions in S2, which is lacking in S1 as we elaborate in Discussion.

----- Fig 11 around here -----

----- Fig 12 around here -----

Discussion

In this paper, we examined local field potentials (LFPs) recorded from primary and secondary somatosensory cortex (S1 and S2) of anesthetized cats. Our four main findings are: 1) as to fundamental frequencies, we found strong LFP responses to both low frequency (*F1*=23Hz) and high frequency (*F2*=200Hz), with strong main effect and some interaction (Figs 1 and 2), 2) as to harmonic and intermodulation frequencies, we found strong evidence of nonlinear processing in the somatosensory pathway (Figs 1 and 2) which were further analyzed with our computational modeling (Figs 9-12), 3) as to the spatial properties of these response, we found that they were highly spatially localized, often showing sharp response boundaries in cortical locations and isolated areas of strong responses (Figs 3-5), 4) as to the nontagged broadband (50-150Hz) high gamma power (HGP), we found evidence to question the validity of the assumption that is used to compute signal-to-noise ratio in SSEP paradigm [3, 4] observed in S2. (Figs 6-8). In the following, we will discuss each of these points in detail.

Responses at fundamental frequencies (*f1*=23Hz and *f2*=200Hz)

We observed strong main effects and interactions of input stimulus amplitudes (Fig 2) at both low and high frequencies. In terms of the proportions of the recorded sites, roughly 4% and 12% of sites responded at 23Hz and 200Hz.

The dominance of the latter response type may be somewhat surprising. Previously, this type of highly narrow band oscillatory responses in LFP have been reported by Rager and Singer [30], who recorded from the visual cortex of anesthetized cats under the SSEP paradigm. However, they reported the LFP responses up to 100Hz, in response to 50Hz visual flickers. Because single neurons have refractory periods, cortical excitatory neurons usually cannot fire at 200Hz. Indeed, in our previous study [16], we did not observe any neurons that fired at that level of high frequency range. Thus, we believe that this 200Hz response is highly unlikely to originate from SUA.

There are at least two possible sources for this 200Hz LFP response, each of which is not mutually exclusive to the other. First is that it reflects high frequency inputs from other areas. LFP is known to reflect synaptic inputs to neurons rather than spiking outputs from neurons [31, 32]. Thus, if the thalamic input to these regions contain a 200Hz component, then the cortical LFP can reflect such high frequency input. Second possibility is that a population of neurons within S1 and S2 spikes in phase at 200Hz modulation [33]. In other words, while each neuron does not spike at 200Hz, population spiking is observed at 200Hz. 200Hz inputs from other areas are likely to induce subthreshold oscillation, which modulates the probability of spikes occurring in phase. This can also generate 200Hz LFP responses. As our study is not primarily designed to test these possibilities, it is not possible to draw a firm conclusion as to whether

these two possibilities are sufficient (or other mechanisms play a significant role) or which possibility is dominant. Future studies are needed.

Another feature of LFP responses at fundamental frequencies is the interaction effects of both *F1* and *F2* input stimulus amplitude, which is significant at ~5% of the recorded sites (Fig 2C at both 23Hz and 200Hz responses). Clear examples of this response at single recording sites are demonstrated in Fig 5A. The interaction effects are visible in some recording sites. These interaction effects were also reported in our previous paper at the SUA level (Figs 5C-5H of [16]). For example, some SUA exhibited linear increase as the amplitude of *F1*=23Hz increases, when *F2*=200Hz amplitude is 0, while the same SUA did not vary at all when *F2*=200Hz amplitude was varied, in the absence of *F1*=23Hz modulation. However, this SUA strongly increased its response in the presence of *F2*=200Hz. Such an interaction effect of SUAs can be explained by subthreshold oscillation and nonlinear thresholding. It is plausible that *F2*=200Hz does not generate sufficiently strong input to a neuron to make it fire but the stimulus induces strong subthreshold oscillation, which can modulate the firing rate. This is consistent with cortical single unit analysis suggesting that high frequency drive from Pacinian corpuscle afferents has a net balanced excitatory-inhibitory drive but accounts for high frequency fluctuations in the cortical responses of many neurons [34]. Yet another possible explanation can be offered based on our LFP findings. Assuming that LFP already reflects the input from the lower thalamic areas, the above subthreshold-interaction effects are already at play in the thalamus and the interaction effects seen at S1 and S2 is just reflection of this interaction effects of thalamic neurons' spikes. Again, our experiment was not designed to test this hypothesis, thus it requires further studies to test this idea.

Evidence for nonlinear processing of somatosensory pathway

We observed strong harmonic and intermodulation (IMs) responses in both S1 and S2 across various response frequencies. While harmonic responses in LFPs have been reported previously [30], we are not aware of the reports on IM responses in LFP (for electrocorticogram, see [35 Verghese 2017 Journal of Neuroscience]. For review of intermodulations, see [15]).

Harmonic responses at LFPs can result from purely sinusoidal spiking input modulation to a given neuron, if the synaptic input response (either excitatory postsynaptic potential or inhibitory postsynaptic potential) have non-sinusoidal form. Thus, it is not extremely informative in inferring the local neural circuit property.

On the other hand, the presence or absence of IMs are potentially quite useful. EEG studies combined with computational modeling [2, 36-38] have used IMs to distinguish potential architecture of the neural computation. In our recording at the level of LFPs, the IMs responses are often observed as indicated by blue lines along the *x*-axis in Fig 2.

Building on this empirical finding, we proceeded with the computational modeling studies (Figs 9-12). We tried to infer potential neural processes for the observed nonlinear responses by comparing some models with respect to their fitting performance. Based on the past literature, here we focused on the rectification and square wave as the primary mechanisms, which are biologically plausible [15]. Overall, the quality of the model fitting was quite obviously better with the rectification model, while it was poor with the square wave model in most channels (Figs 11 and 12 and Sup Fig 5). Further, integrative nonlinear computations were strongly implicated in our modelling in particular for S2 (Figs 11 and 12). A possible implementation of rectification at

632 the neural circuits could be the one of phase insensitive mechanisms, such as complex cells
633 found in the visual cortex [39]. We are not aware of specific models in the somatosensory
634 system which would correspond to complex cells in the visual system. Meanwhile, the
635 multiplication of two rectification functions can be implemented by coincidence-detector
636 mechanisms, which has been found in the barn owl sound-localization system [40]. Coincidence
637 detectors would integrate the inputs from two functions and become active in an *AND* gate like
638 operation in a biologically plausible way. Again, we are not aware of direct evidence for
639 coincidence-detectors in the somatosensory system.
640
641 Regardless of the precise mechanisms, our modelling analysis implicates that such
642 mechanisms are likely to be primarily at play in S2, but not S1. While integration of the neural
643 activity has been hypothesized to occur primarily in S2 than S1 on an anatomical basis, we
644 believe our demonstration is the first to claim this on a computational basis. While highly
645 intriguing, further works are needed to examine what actual neural mechanisms generate these
646 responses in order to evaluate the usefulness of our computational modeling with IM
647 components [15].
648

649 Local nature of SSEP responses

650 Steady state responses are most often utilized in cognitive neuroscience, typically with
651 electroencephalography (EEG) or magnetoencephalography (MEG) performed on humans [3, 4]
652 (but also see [1]), and predominantly using visual stimuli at relatively low frequency range (but
653 also see [41]).
654
655 While there are some attempts to localize the source of SSEPs, due to the limitation of scalp
656 recording, the SSEP's resolutions are still at the level of >cm. Compared to such coarse

resolution, the spatial resolution of our findings from Figs 3-5 and 7 is quite striking. Our spatial resolution was potentially enhanced by bipolar re-referencing [17, 42] and may reflect highly localized clusters of neurons or synaptic inputs to such neurons. The isolated response patterns in Figs 3-5 and 7 suggest that such localized circuitry may exist in a submillimeter scale, the spacing of our array electrodes. Combining with a dense EEG/MEG/ECoG recording, the usage of SSEP paradigm may be able to push the limit of spatial resolution of the source localization for these techniques, by targeting highly localized neural circuits within the human brain. Given the recent explosion of brain machine interface applications that utilize the SSEP paradigm [3], an improved spatial resolution of SSEP can have broader implications outside of the basic science, extending to the field of engineering and clinical neuroscience.

High gamma power (HGP) responses in S2 and log*SNR* computation

Outside of the tagged frequencies (fundamental, harmonics, and IMs), we initially expected that LFP power spectra can be regarded as noise, as is usually assumed in SSEP literature [3, 4]. However, we found that this assumption was not really met in some channels (~5%) within S2 (Fig 6). While broadband (50-150Hz) HGP has been reported in many studies that analyzed ECoG [43-45] and LFPs [46], they tend to be short-lived and may not be relevant for log*SNR* computation if only the sustained components are used. However, our S2 HGP were in fact sustained and at the comparable magnitude with those at the harmonic and intermodulation frequencies (Fig 8).

We are not sure why HGP was completely absent in S1. Along with the above modeling results, the presence or absence of HGP was a prominent difference between S1 and S2. This

difference in HGP might be partially explained by the difference in recording electrodes (planar array for S1 and linear array for S2).

While the exact reason of the presence of HGP in S2 but not in S1 remains puzzling, our results at least provide a cautionary note on the practice of log*SNR* computation, which assumes that evoked SSEP responses can be quantified by comparisons of the power at a given stimulation frequency f and its neighbors. Neighboring non-stimulation frequencies can indeed change its response magnitude in the SSEP paradigm.

Conclusion

Taken together, our SSEP analyses with LFP revealed nonlinear processing in somatosensory cortex, which is likely to be hierarchically organized. Our results constrain the computational and hierarchical organization of S1 and S2, implying S2 integrates oscillatory functions in a nonlinear way. While this paper focused on a simple Fourier transform of the LFPs, interactions among simultaneously recorded LFPs can be further analyzed by other types of spectral-domain techniques, ranging from coherency [47], Granger causality [48, 49], and integrated information [50]. Given the rich information present in LFPs, which reflects the local neural circuit properties, especially IMs [15], this type of high resolution LFP recordings from animal models can serve as quite powerful tools to dissect the functional and computational properties of underlying circuitries of neural systems across sensory modalities.

Acknowledgements

We thank Prof Trichur Vidyasagar for his insightful comments. This work was supported by the MASSIVE HPC facility (www.massive.org.au).

References

1. Regan D, Regan MP. Objective evidence for phase-independent spatial frequency analysis in the human visual pathway. Vision research (Oxford). 1988;28(1):187-91. doi: 10.1016/S0042-6989(88)80018-X.
2. Regan MP, Regan D. A frequency domain technique for characterizing nonlinearities in biological systems. Journal of theoretical biology. 1988;133(3):293-317. doi: 10.1016/S0022-5193(88)80323-0.
3. Vialatte F-B, Maurice M, Dauwels J, Cichocki A. Steady-state visually evoked potentials: focus on essential paradigms and future perspectives. Progress in neurobiology. 2010;90(4):418. doi: 10.1016/j.pneurobio.2009.11.005.
4. Norcia AM, Appelbaum LG, Ales JM, Cottereau BR, Rossion B. The steady-state visual evoked potential in vision research: A review. Journal of vision. 2015;15(6):4. doi: 10.1167/15.6.4.
5. Rossion B. Understanding face perception by means of human electrophysiology. Trends in cognitive sciences. 2014;18(6):310-8. doi: 10.1016/j.tics.2014.02.013.
6. Gordon N, Koenig-Robert R. Neural markers of predictive coding under perceptual uncertainty revealed with Hierarchical Frequency Tagging. eLife. 2017;6. doi: 10.7554/eLife.22749.
7. Koenig-Robert R, Vanrullen R, Tsuchiya N. Semantic Wavelet-Induced Frequency-Tagging (SWIFT) Periodically Activates Category Selective Areas While Steadily Activating Early Visual Areas. PloS one. 2015;10(12):e0144858. doi: 10.1371/journal.pone.0144858.
8. Cohen D, Zalucki OH, van Swinderen B, Tsuchiya N. Local Versus Global Effects of Isoflurane Anesthesia on Visual Processing in the Fly Brain. eneuro. 2016;3(4):ENEURO.0116-16.2016-16. doi: 10.1523/ENEURO.0116-16.2016.

9. Clynes M. Unidirectional rate sensitivity: a biocybernetic law of reflex and humoral systems as physiologic channels of control and communication. Annals of the New York Academy of Sciences. 1961;92:946.

10. Zemon V, Ratliff F. Intermodulation components of the visual evoked potential: Responses to lateral and superimposed stimuli. Biological Cybernetics. 1984;50(6):401-8. doi: 10.1007/BF00335197.

11. Boremanse A, Norcia AM, Rossion B. An objective signature for visual binding of face parts in the human brain. Journal of vision. 2013;13(11). doi: 10.1167/13.11.6.

12. Zhang P, Jamison K, Engel S, He B, He S. Binocular Rivalry Requires Visual Attention. Neuron (Cambridge, Mass). 2011;71(2):362-9. doi: 10.1016/j.neuron.2011.05.035.

13. Gundlach C, Müller MM. Perception of illusory contours forms intermodulation responses of steady state visual evoked potentials as a neural signature of spatial integration. Biological psychology. 2013;94(1):55-60. doi: 10.1016/j.biopsycho.2013.04.014.

14. Gordon N, Tsuchiya N, Koenig-Robert R, Hohwy J. Expectation and attention increase the integration of top-down and bottom-up signals in perception through different pathways.(Research Article). PLoS Biology. 2019;17(4):e3000233. doi: 10.1371/journal.pbio.3000233.

15. Gordon N, Hohwy J, Davidson MJ, van Boxtel JJA, Tsuchiya N. From intermodulation components to visual perception and cognition-a review. NeuroImage (Orlando, Fla). 2019;199:480-94. doi: 10.1016/j.neuroimage.2019.06.008.

16. Carter AW, Chen SC, Lovell NH, Vickery RM, Morley JW. Convergence across tactile afferent types in primary and secondary somatosensory cortices. PloS one. 2014;9(9):e107617. doi: 10.1371/journal.pone.0107617.

17. Cohen D, Tsuchiya N. The Effect of Common Signals on Power, Coherence and Granger Causality: Theoretical Review, Simulations, and Empirical Analysis of Fruit Fly LFPs Data. Frontiers in Systems Neuroscience. 2018;12. doi: 10.3389/fnsys.2018.00030.

757 18. Mitra P. Observed brain dynamics. Bokil H, Ebooks C, editors. New York
758 Oxford: New York
759 Oxford : Oxford University Press; 2008.
760 19. Canolty R, Edwards E, Dalal S, Soltani M. High Gamma Power Is Phase-Locked to
761 Theta Oscillations in Human Neocortex. Science. 2006;313(5793):1626-8. doi:
762 10.1126/science.1128115.
763 20. György B, Costas AA, Christof K. The origin of extracellular fields and currents — EEG,
764 ECoG, LFP and spikes. Nature Reviews Neuroscience. 2012;13(6):407. doi: 10.1038/nrn3241.
765 21. Ray S, Crone NE, Niebur E, Franaszczuk PJ, Hsiao SS. Neural correlates of high-
766 gamma oscillations (60-200 Hz) in macaque local field potentials and their potential implications
767 in electrocorticography. The Journal of neuroscience : the official journal of the Society for
768 Neuroscience. 2008;28(45):11526. doi: 10.1523/JNEUROSCI.2848-08.2008.
769 22. Ray S, Maunsell JHR. Different Origins of Gamma Rhythm and High-Gamma Activity in
770 Macaque Visual Cortex (Different Origins of γ and High-γ). PLoS Biology. 2011;9(4):e1000610.
771 doi: 10.1371/journal.pbio.1000610.
772 23. Benjamini Y, Hochberg Y. Controlling the False Discovery Rate: A Practical and
773 Powerful Approach to Multiple Testing. Journal of the Royal Statistical Society: Series B
774 (Methodological). 1995;57(1):289-300. doi: 10.1111/j.2517-6161.1995.tb02031.x.
775 24. Delorme A, Makeig S. EEGLAB: an open source toolbox for analysis of single-trial EEG
776 dynamics including independent component analysis. Journal of neuroscience methods.
777 2004;134(1):9-21. doi: 10.1016/j.jneumeth.2003.10.009.
778 25. Lachaux J-P, Axmacher N, Mormann F, Halgren E, Crone NE. High-frequency neural
779 activity and human cognition: Past, present and possible future of intracranial EEG
780 research.(Report). Progress in Neurobiology. 2012;98(3):279. doi:
781 10.1016/j.pneurobio.2012.06.008.

26. Gabbiani F, Krapp HG, Hatsopoulos N, Mo C-H, Koch C, Laurent G. Multiplication and stimulus invariance in a looming-sensitive neuron. Journal of physiology, Paris. 2004;98(1-3):19-34. doi: 10.1016/j.jphysparis.2004.03.001.

27. Peña JL, Konishi M. Robustness of multiplicative processes in auditory spatial tuning. The Journal of neuroscience : the official journal of the Society for Neuroscience. 2004;24(40):8907.

28. Burnham KP, Anderson DR. Multimodel Inference: Understanding AIC and BIC in Model Selection. Sociological Methods & Research. 2004;33(2):261-304. doi: 10.1177/0049124104268644.

29. Scales LE. Introduction to non-linear optimization. New York: New York : Springer-Verlag; 1985.

30. Rager G, Singer W. The response of cat visual cortex to flicker stimuli of variable frequency. European Journal of Neuroscience. 1998;10(5):1856-77. doi: 10.1046/j.1460-9568.1998.00197.x.

31. Mitzdorf U. Properties of the evoked potential generators: current source-density analysis of visually evoked potentials in the cat cortex. Int J Neurosci. 1987;33(1-2):33-59. Epub 1987/03/01. doi: 10.3109/00207458708985928. PubMed PMID: 3610492.

32. Nikos KL, Jon P, Mark A, Torsten T, Axel O. Neurophysiological investigation of the basis of the fMRI signal. Nature. 2001;412(6843):150. doi: 10.1038/35084005.

33. Harvey MA, Saal HP, Dammann JF, III, Bensmaia SJ. Multiplexing stimulus information through rate and temporal codes in primate somatosensory cortex.(Report). PLoS Biology. 2013;11(5). doi: 10.1371/journal.pbio.1001558.

34. Saal HP, Harvey MA, Bensmaia SJ. Rate and timing of cortical responses driven by separate sensory channels.(Report). eLife. 2015;4(2015). doi: 10.7554/eLife.10450.

35. Kim Y-J, Tsai JJ, Ojemann J, Verghese P. Attention to Multiple Objects Facilitates Their Integration in Prefrontal and Parietal Cortex. The Journal of neuroscience : the official journal of the Society for Neuroscience. 2017;37(19):4942. doi: 10.1523/JNEUROSCI.2370-16.2017.

36. Baker DH, Wade AR. Evidence for an Optimal Algorithm Underlying Signal Combination in Human Visual Cortex. Cerebral cortex (New York, NY : 1991). 2017;27(1):254. doi: 10.1093/cercor/bhw395.

37. Cunningham DGM, Baker DH, Peirce JW. Measuring nonlinear signal combination using EEG. Journal of vision. 2017;17(5):10. doi: 10.1167/17.5.10.

38. Tsai JJ, Wade AR, Norcia AM. Dynamics of normalization underlying masking in human visual cortex. The Journal of neuroscience : the official journal of the Society for Neuroscience. 2012;32(8):2783. doi: 10.1523/JNEUROSCI.4485-11.2012.

39. Hubel DH, Wiesel TN. Receptive fields of single neurones in the cat's striate cortex. The Journal of physiology. 1959;148:574.

40. Carr CE, Konishi M. Axonal delay lines for time measurement in the owl's brainstem. Proceedings of the National Academy of Sciences of the United States of America. 1988;85(21):8311. doi: 10.1073/pnas.85.21.8311.

41. Herrmann CS. Human EEG responses to 1–100 Hz flicker: resonance phenomena in visual cortex and their potential correlation to cognitive phenomena. Experimental Brain Research. 2001;137(3-4):346-53. doi: 10.1007/s002210100682.

42. Shirhatti V, Borthakur A, Ray S. Effect of Reference Scheme on Power and Phase of the Local Field Potential. Neural Computation. 2016;28(5):1-32. doi: 10.1162/NECO_a_00827.

43. Crone NE, Miglioretti DL, Gordon B, Lesser RP. Functional mapping of human sensorimotor cortex with electrocorticographic spectral analysis. II. Event-related synchronization in the gamma band. Brain. 1998;121(12):2301-15. doi: 10.1093/brain/121.12.2301.

44. Miller KJ, Zanos S, Fetz EE, Den Nijs M, Ojemann JG. Decoupling the cortical power spectrum reveals real-time representation of individual finger movements in humans. The Journal of neuroscience : the official journal of the Society for Neuroscience. 2009;29(10):3132. doi: 10.1523/JNEUROSCI.5506-08.2009.

45. Tsuchiya N, Kawasaki H, Oya H, Howard MA, Adolphs R. Decoding Face Information in Time, Frequency and Space from Direct Intracranial Recordings of the Human Brain (Decoding Faces in ECoG). PLoS ONE. 2008;3(12):e3892. doi: 10.1371/journal.pone.0003892.

46. Ray S, Maunsell JHR. Differences in Gamma Frequencies across Visual Cortex Restrict Their Possible Use in Computation. Neuron (Cambridge, Mass). 2010;67(5):885-96. doi: 10.1016/j.neuron.2010.08.004.

47. Jarvis MR, Mitra PP. Sampling Properties of the Spectrum and Coherency of Sequences of Action Potentials. Neural Computation. 2001;13(4):717-49. doi: 10.1162/089976601300014312.

48. Cohen D, van Swinderen B, Tsuchiya N. Isoflurane Impairs Low-Frequency Feedback but Leaves High-Frequency Feedforward Connectivity Intact in the Fly Brain. eneuro. 2018;5(1):ENEURO.0329-17.2018-17. doi: 10.1523/ENEURO.0329-17.2018.

49. Dhamala M, Rangarajan G, Ding M. Analyzing information flow in brain networks with nonparametric Granger causality. NeuroImage (Orlando, Fla). 2008;41(2):354-62. doi: 10.1016/j.neuroimage.2008.02.020.

50. Cohen D, Sasai S, Tsuchiya N, Oizumi M. A general spectral decomposition of causal influences applied to integrated information. Journal of neuroscience methods. 2020;330. doi: 10.1016/j.jneumeth.2019.108443.

Figures

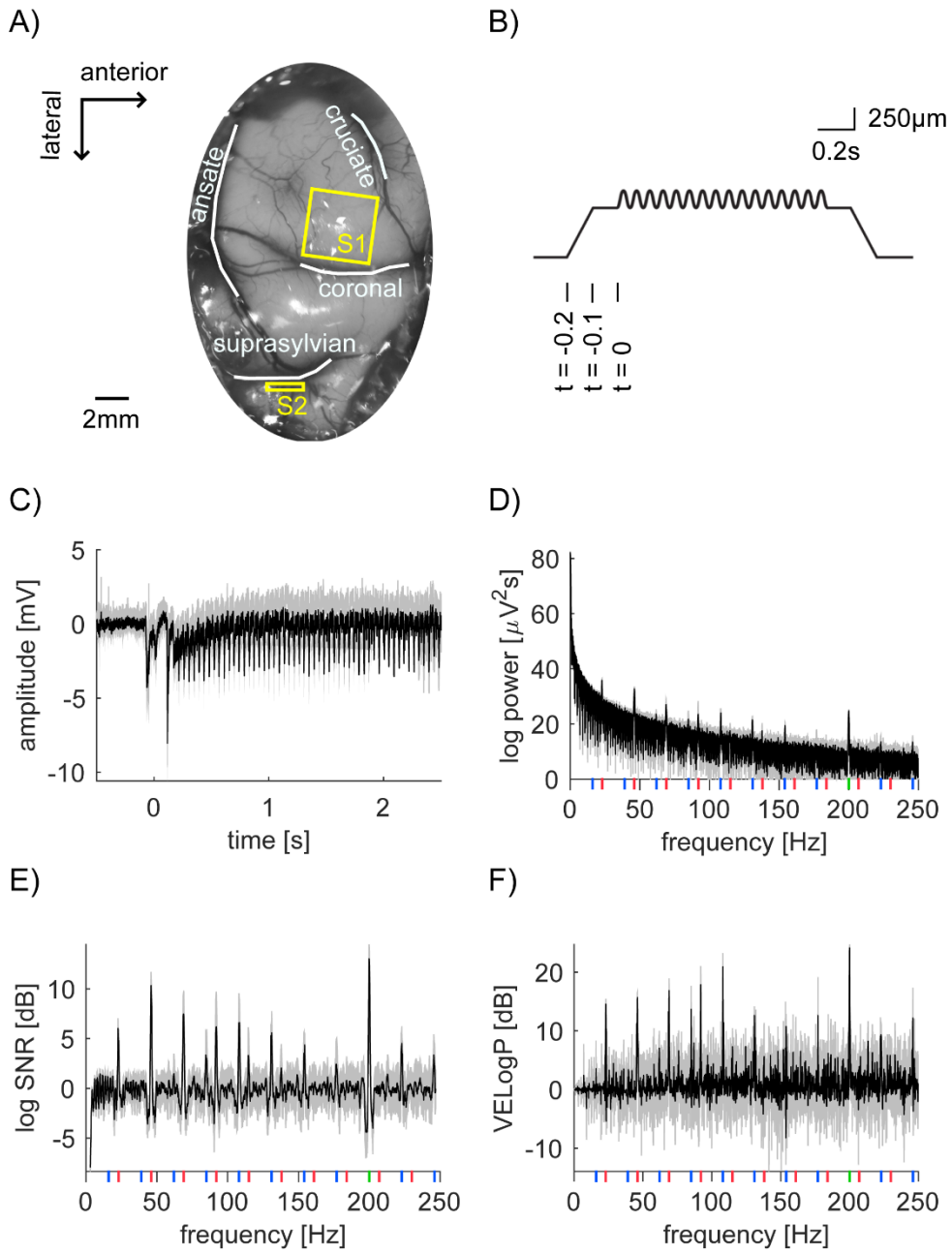

Fig 1. Neural recording, vibratory stimulation and our analysis scheme.

(A) Photo of anterior parietal cortex with outlines of sulci (white lines) superimposed. The planar array was inserted into the paw representation region of S1 (yellow square). A linear array was inserted into S2 region located in the suprasylvian sulci (yellow rectangle). (B) Time course of the depth modulation of the vibratory stimulation. The stimulator presses 500μm into the skin

over 0.1s of ramping, followed by a pause of 0.1s. At *t*=0, the vibration stimulation starts. Here, 159μm of 23Hz sinusoid is superimposed on a step indentation. We represent a combination of the depth modulation for *F1* and *F2*, such as *X* [μm] and *Y* [μm], as [*F1*, *F2*]=[*X, Y*]. (C) Time domain representation of LFP signal from bipolar channel 156 in S1 (Session 2-2). Here, we computed the mean of the pre-stimulus LFP from -0.5 to -0.1s and used it as a baseline per trial, which is subtracted from LFP per trial. The mean trace from 15 trials is shown ([*F1*, *F2*]=[159, 16]). Shade represents the standard "deviation" across 15 trials, indicating extremely robust and clean SSEP. (D) Power spectrum of the LFP signal from 0.5 to 2.5s after stimulus onset in (C). Again, shading represents standard "deviation". Vertical lines show frequencies of interest. (Red for 23Hz and its harmonics, green for 200Hz and blue for intermodulation.) (E and F) Frequency domain representation of log*SNR* (E) and vibration evoked logPower (VELogP) (F).

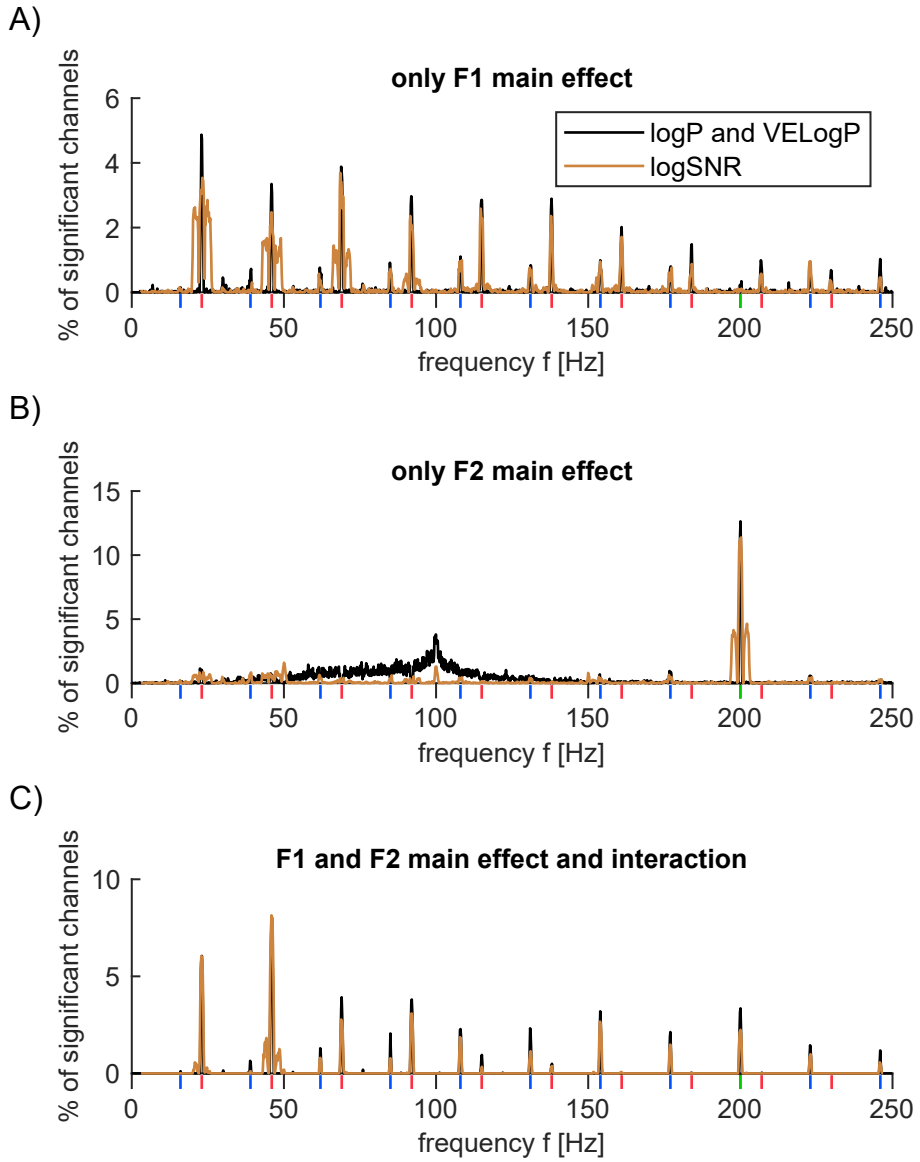

Fig 2. Proportion of significant channels (two-way ANOVA) in S1 and S2. Statistical results from log*P* and *VELogP* are identical and shown in black. Results from log*SNR* are shown in brown. Vertical lines beneath *x*-axis indicate *F1* fundamental and harmonic (red), *F2* fundamental (green), and intermodulation frequencies (blue). (A-C) % of channels that were deemed as significant according to two-way ANOVA only for the main effects of the amplitude of *F1* (but not *F2* main effect nor *F1-F2* interaction; A), *F2*=200Hz main effect only (but not *F1* main effect nor *F1-F2* interaction; B) and both main effects of *F1* and *F2* as well as *F1-F2* interaction (C).

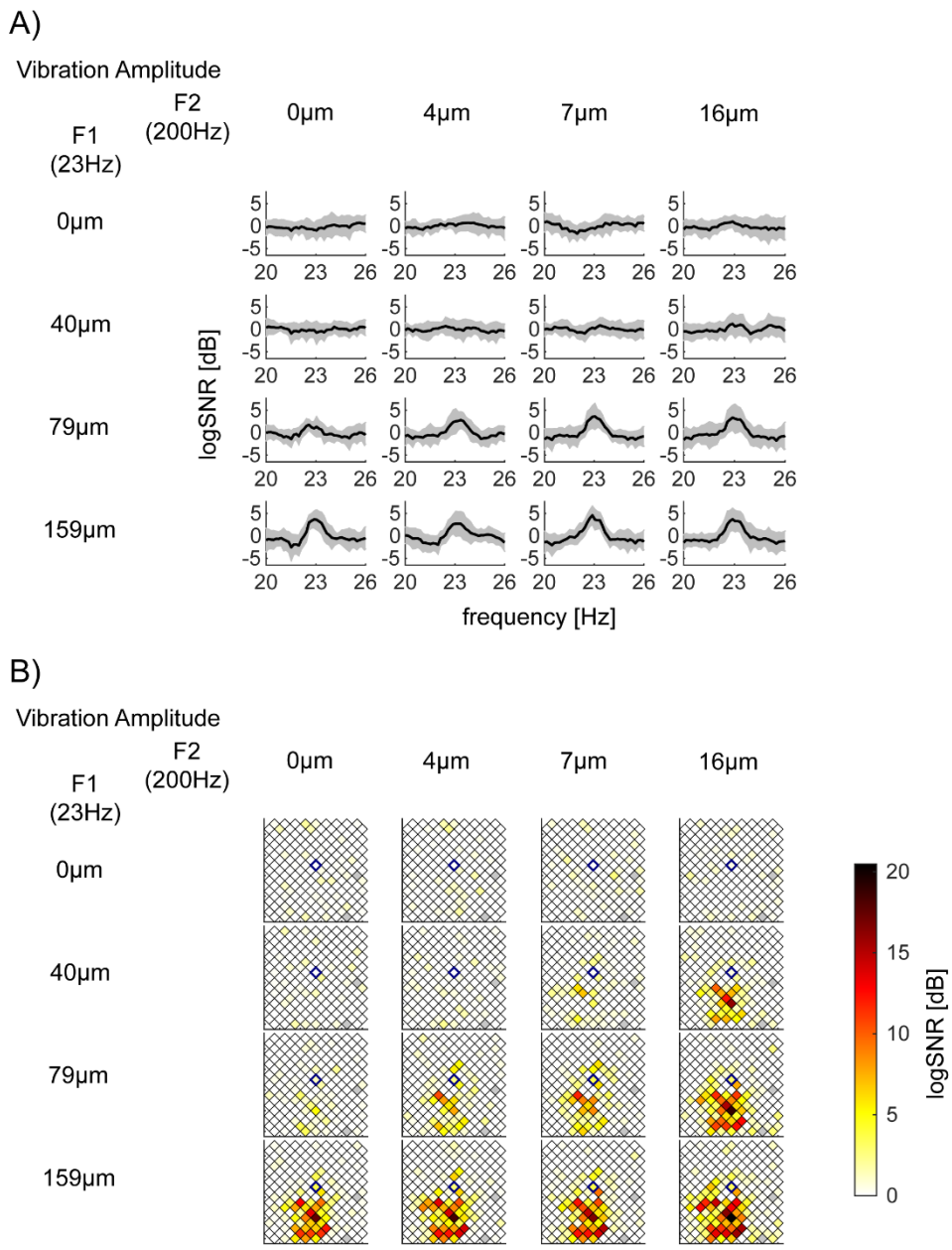

Fig 3. Exemplar log*SNR* at *f1*=23Hz depend on the vibration amplitude of *F1*=23Hz. 16 panels are arranged so that the row and column encodes the input amplitude of *F1*=23Hz (from 0 to 159μm) and *F2*=200Hz (from 0 to 16μm), respectively. (A) log*SNR* of S1 bipolar channel 131, whose location in the Utah array in (B) is identified with a blue diamond, (Session 2-2). This channel's responses at *f1*=23Hz showed a significant main effect of *F1*=23Hz amplitude, but neither the main effect of *F2*=200Hz nor their interaction. *p*-value (*F1*, *F2*,

interaction) = ($<10^{-5}$, 0.054, 0.52) with the corrected threshold 0.00019. *y*-axis of each subplot is the mean log*SNR* with standard deviation across 15 trials. *x*-axis is the response frequency *f*, around *f*=23Hz. (B) Spatial mapping of log*SNR* at *f1*=23Hz across all channels in S1 (Session 2-2). Each square represents one of the bipolar re-referenced channels. The center of the square is plotted at the middle point between the original unipolar recordings of the 10x10 array. Squares with gray indicate channels, which were removed from the analysis (see Methods).

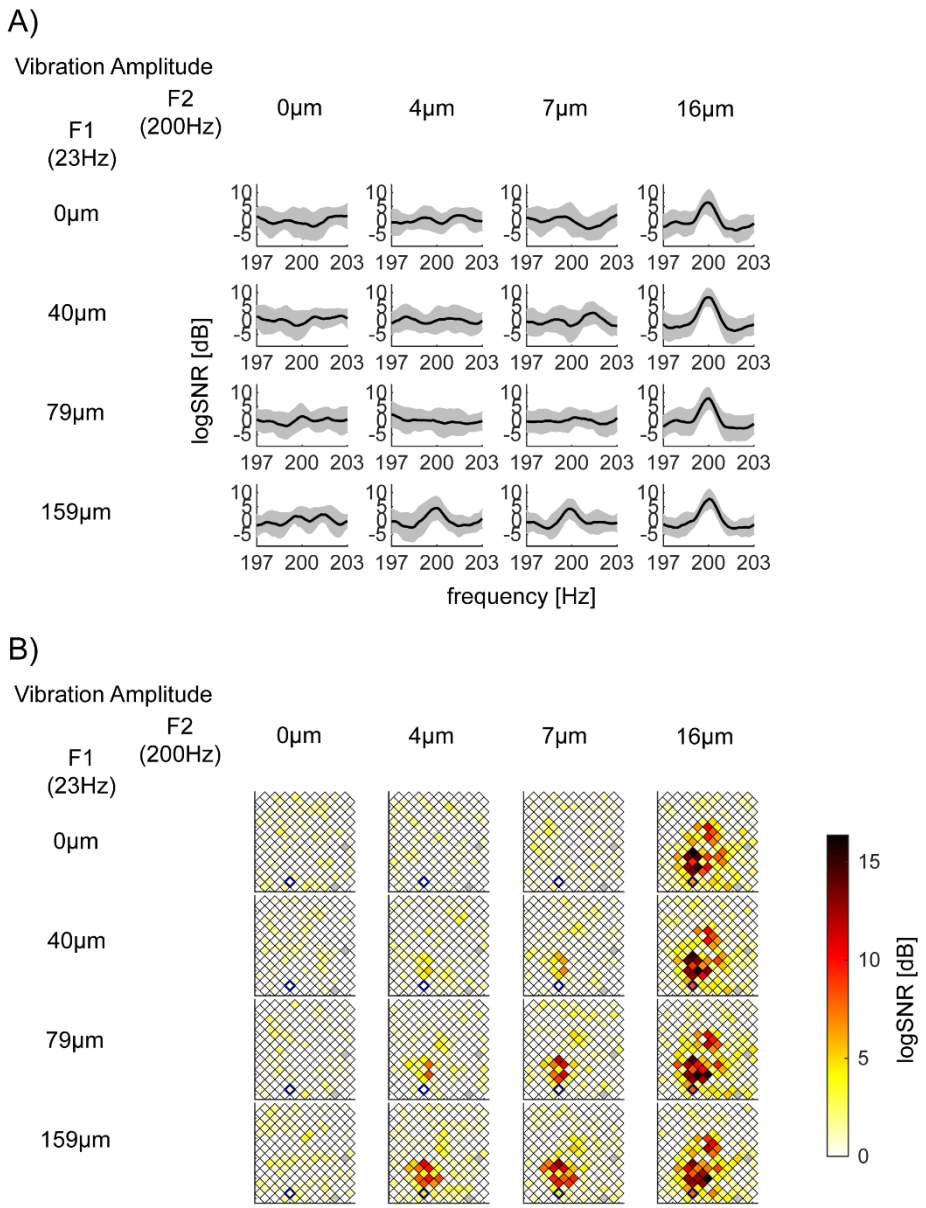

Fig 4. Exemplar log*SNR* at *f2*=200Hz depends on the vibration amplitude of *F2*=200Hz. This figure is shown with the same format as Fig 3. (A) log*SNR* of bipolar channel 36 in S1 (Session 2-2). This channel's responses at *f2*=200Hz showed a significant main effect of *F2*=200Hz amplitude, but neither the main effect of *F1*=23Hz nor their interaction. *x*-axis is the response frequency *f*, around *f*=200Hz. *p*-value (*F1*, *F2*, interaction) = (0.00043, $<10^{-5}$, 0.14) with the corrected threshold 0.00019. (B) Spatial mapping of log*SNR* at *f2*=200Hz across all channels in S1 (Session 2-2).

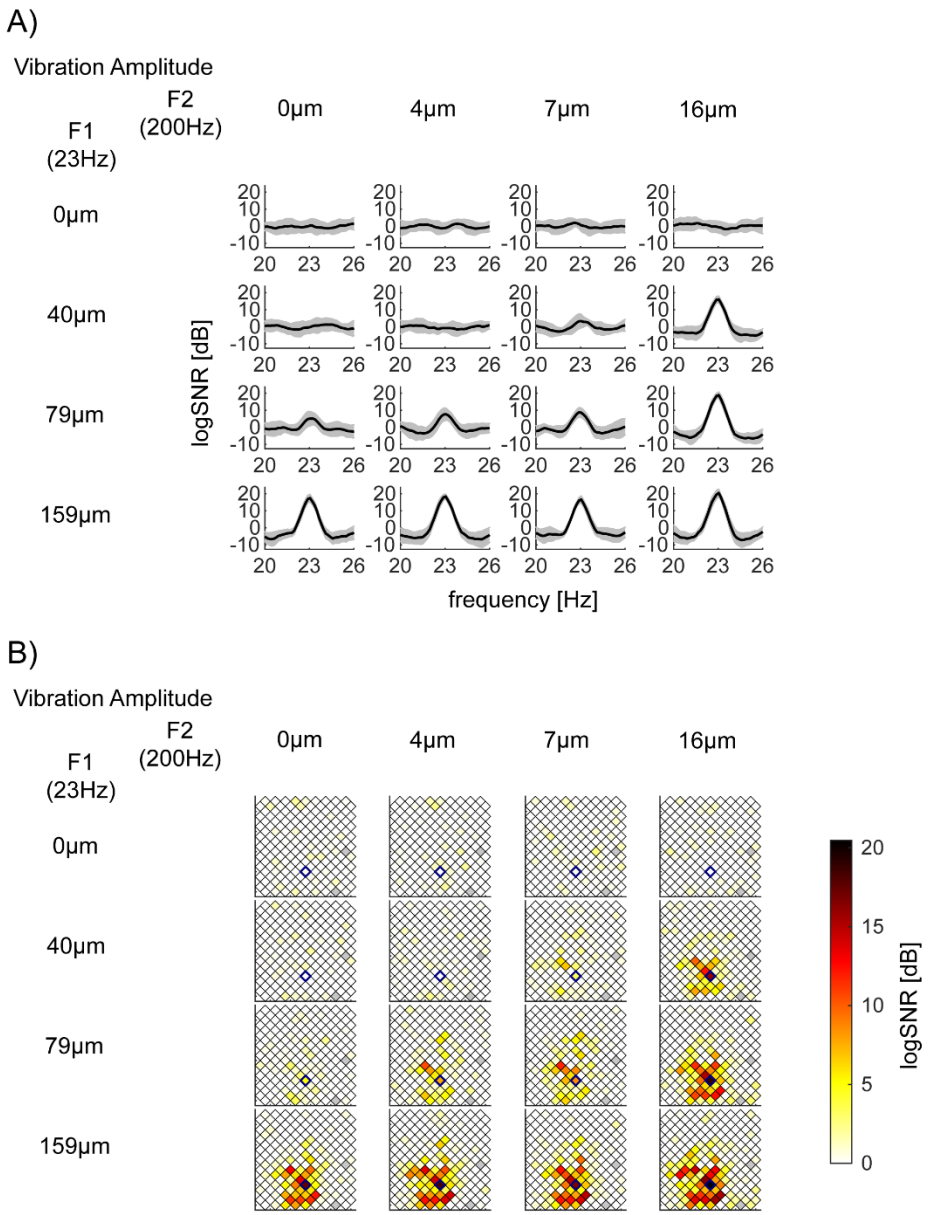

Fig 5. Exemplar log*SNR* at *f1*=23Hz depend on the vibration amplitude of *F1*=23Hz, *F2*=200Hz, and their interaction.

The same format as Fig 3. (A) log*SNR* of bipolar channel 158 in S1 (Session 2-2). This channel's responses at *f1*=23Hz showed a significant main effect of *F1*=23Hz amplitude, the main effect of *F2*=200Hz, and their interaction. *x*-axis is the response frequency *f*, around *f*=23Hz. *p*-values (*F1*, *F2*, interaction) are all $p<10^{-5}$ with the corrected threshold 0.00019. (B) Spatial mapping of log*SNR* at *f2*=200Hz across all channels in S1 (Session 2-2).

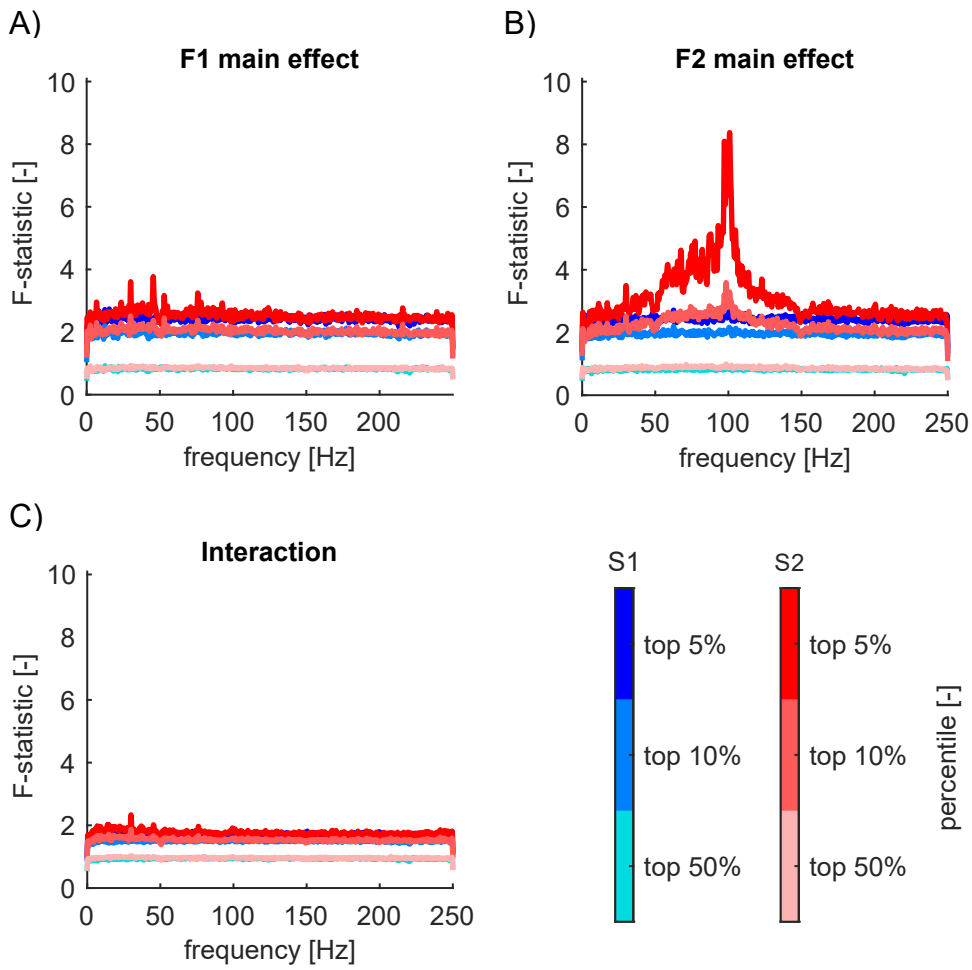

Fig 6. Nontagged frequencies between 50-150Hz in S2 are modulated by *F2*=200Hz vibratory amplitude.

(A)-(C) *F1* main effect (A), *F2* main effect (B), interaction (C) *F*-statistics from ANOVA performed on log*P* in S1 (shades of pale blue to blue) and S2 (shades of pale red to red). We plotted 95th percentile (top 5%), 90th (top 10%), and 50th (median). Some channels in S2 showed significant main effect of 200Hz vibratory amplitude in nontagged frequencies (+/-0.5Hz outside of the tagged, harmonic, and intermodulation frequencies, and outside of 50Hz, 100Hz, and 150Hz) from 50-150Hz. No main effects of 23Hz amplitude or interaction. We smoothed lines for a display purpose (1 data point per 1Hz).

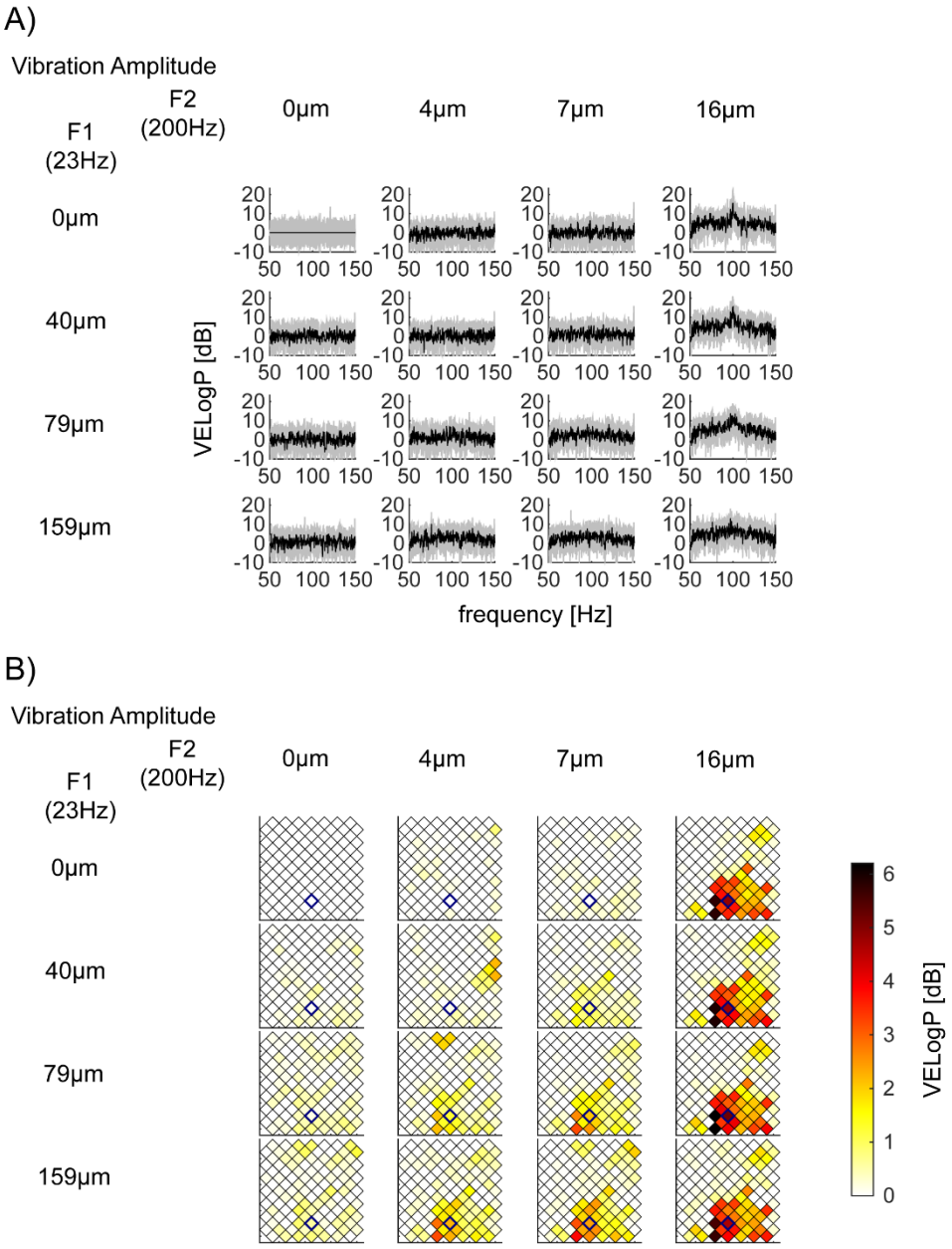

Fig 7. Exemplar nontagged frequencies responses between 50-150Hz modulated by *F2*=200Hz vibratory amplitude.

(A) Exemplar nontagged responses (*VELogP*) between 50-150Hz in bipolar channel 102 in S2 (Session 2-2). (B) Spatial mapping of high gamma power (HGP) in S2 (Session 2-2). The location of bipolar channel 102 is located in the 8x8 array by a blue diamond. Color encodes the mean nontagged HGP in dB (our HGP measure, see Methods).

A)

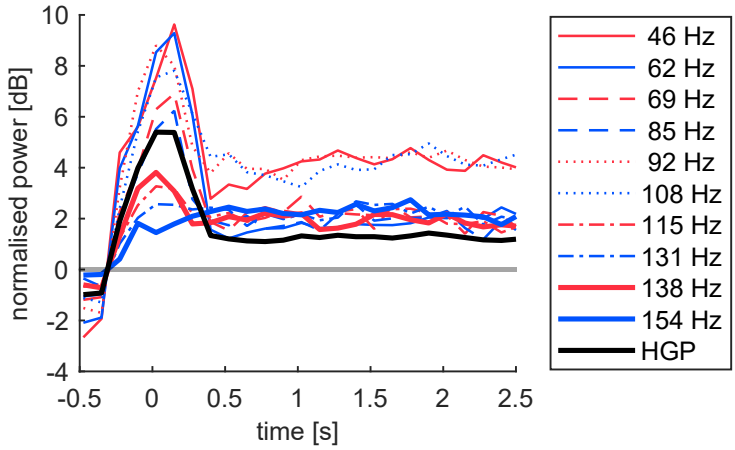

B)

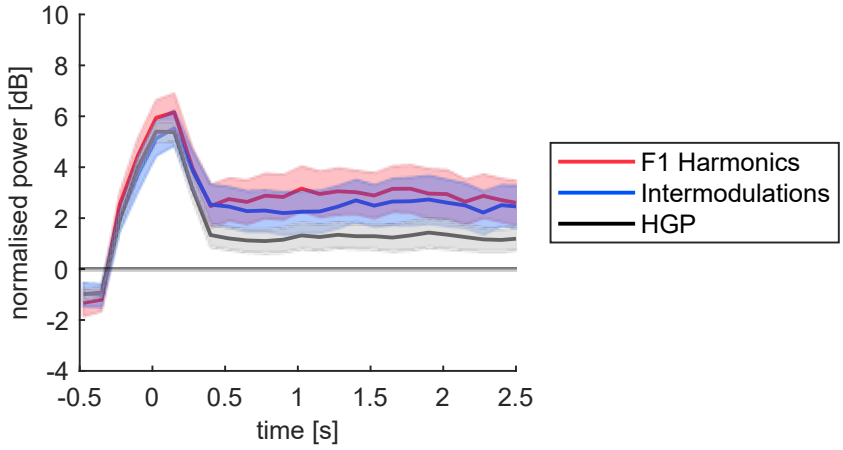

Fig 8. Time course of the mean nontagged HGP and the frequencies of interest in S2. (A) Evoked bandlimited power (half band width=2Hz) around the stimulus onset. Mean log power is first averaged within the frequencies of interest for HGP (thick black), *f1* harmonic (red), and intermodulation (blue) frequencies around HGB for each trial. Different line types for different frequencies (see the legend). Mean across trials per channel is further averaged across channels. The mean power during -0.5 to -0.25s for each frequency per trial is subtracted. (B) Summary of HGP, harmonic and intermodulation frequencies. Time courses for the harmonic (red) intermodulation (blue) in (A) are averaged for each category within each channel. Shading represents standard error of the mean across the top 10% channels selected as in Fig 6.

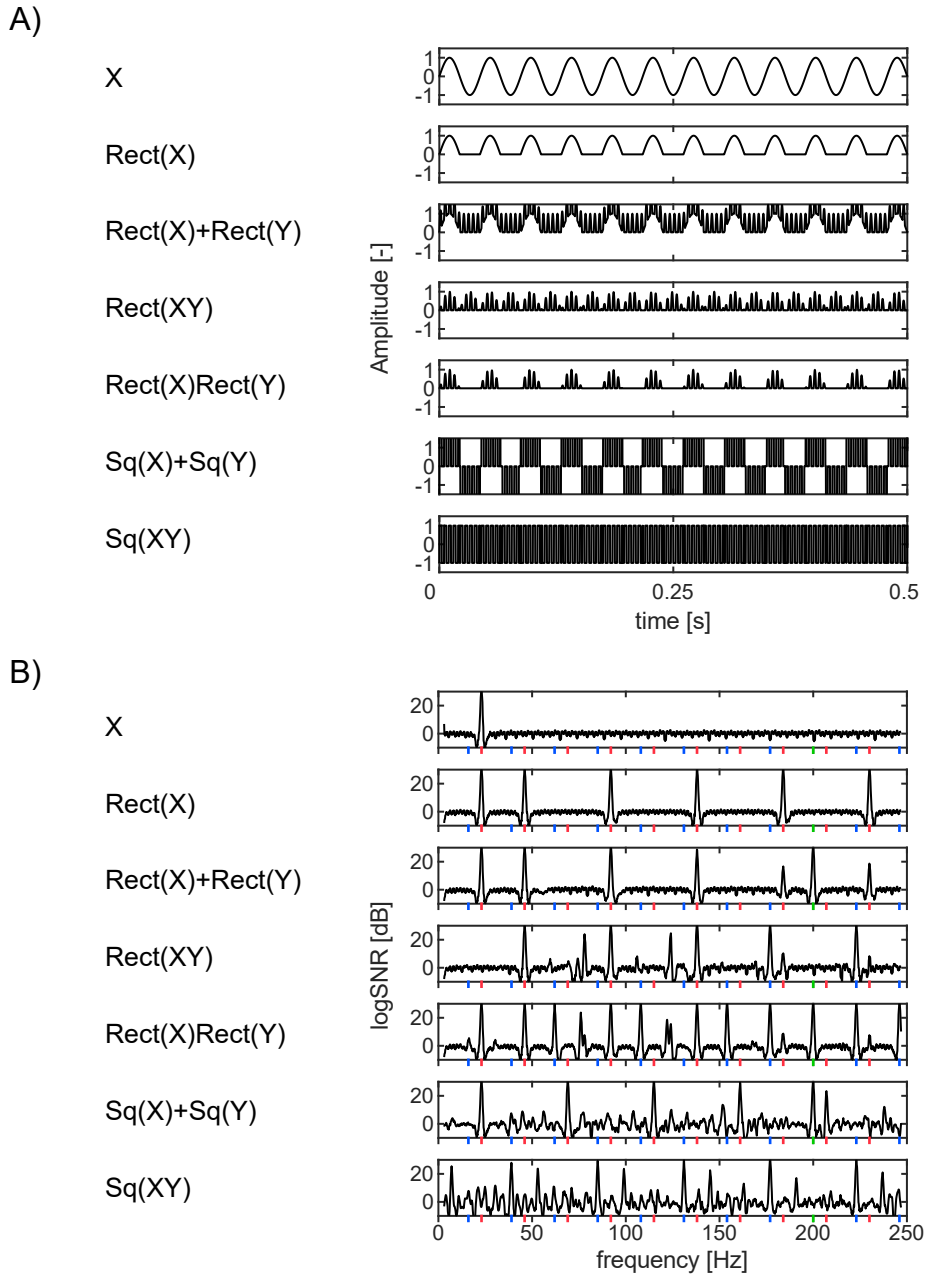

Fig 9. Waveforms of modeled processes.

(A) Waveforms in the time domain (0 to 0.5s). *X* and *Y* are sinusoidal inputs at 23 and 200Hz, respectively. For the definitions of *Rect* and *Sq*, see the main text. (B) Spectra of each waveform in the frequency domain.

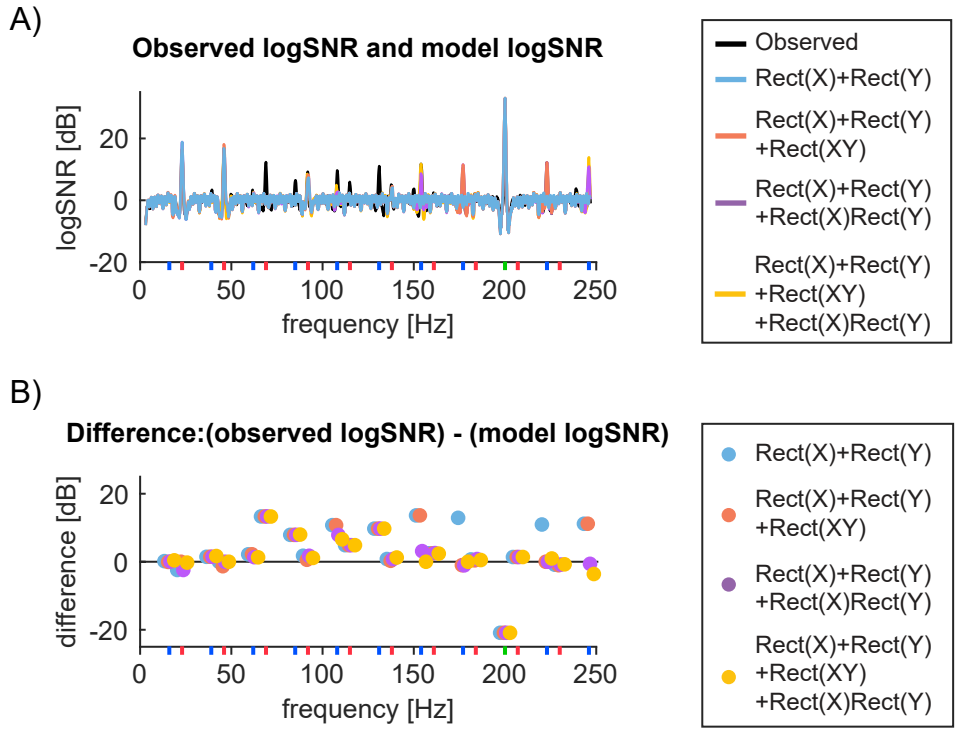

Fig 10. Exemplar channel's observed and modelled responses.

(A) Bipolar channel 43 in S1 (Session 2-2)'s log*SNR* (black) is compared to the optimally fitted models from four model architectures based on *Rect* functions. The best parameters for each model are: (red) -0.023*Rect(X)*+1.0*Rect(Y)*, (blue) -0.98*Rect(X)*+58*Rect(Y)*-0.90*Rect(XY)*, (purple) -0.98*Rect(X)*+30*Rect(X)*+0.094*Rect(X)Rect(Y)* and (yellow) and 1.8*Rect(X)*+55*Rect(Y)*+0.48*Rect(XY)*-2.4*Rect(X)Rect(Y)*. The respective sums of log*SNR* differences from the observed log*SNR* across the frequencies of interest are 130, 105, 83 and 79. (B) Difference between the observed and the best model at the frequencies of interest. Color scheme is the same as in (A).

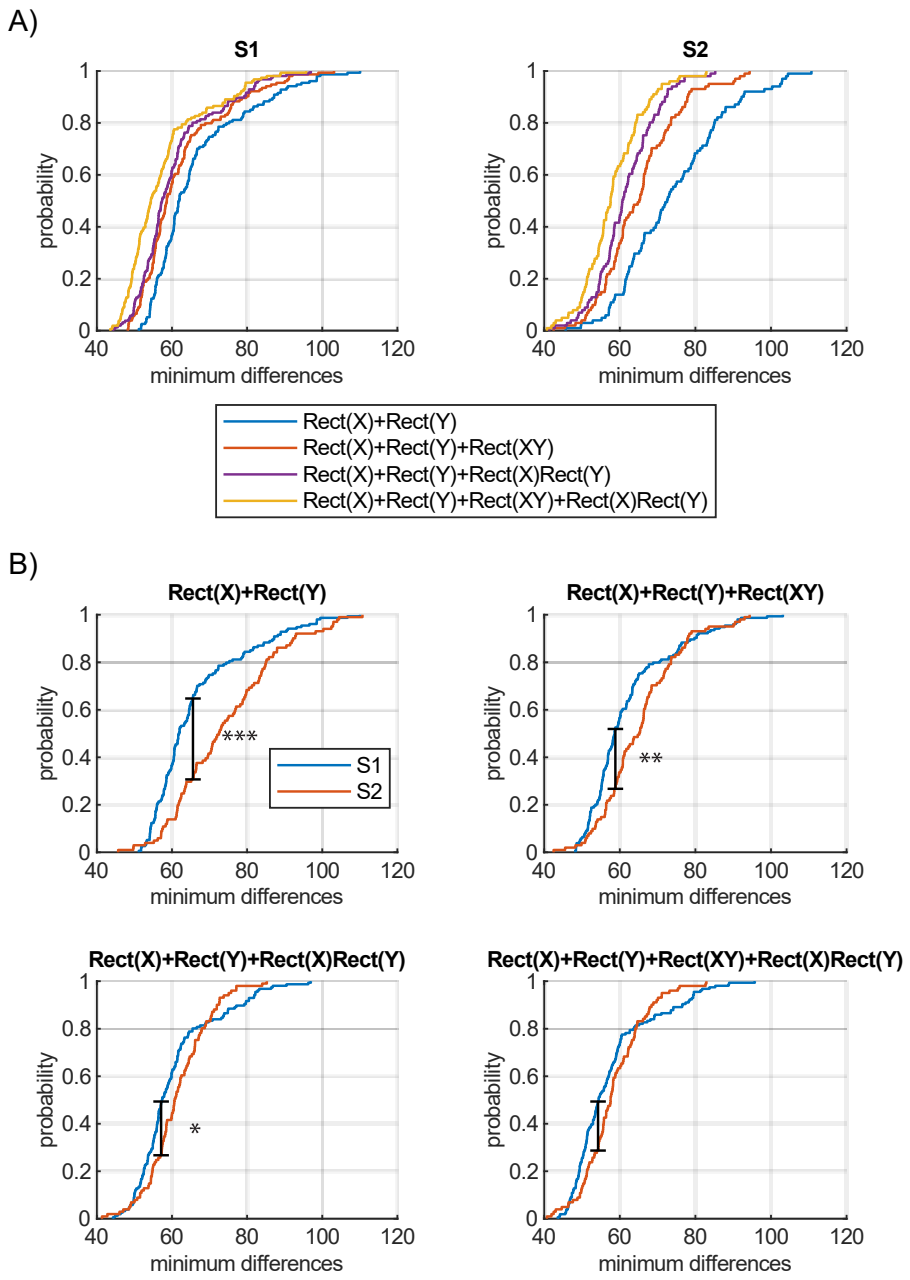

Fig 11. Comparison of fitting performances across rectification models.

(A) Comparison of performance across four rectification models based on the cumulative probability distributions of the minimum difference for S1 and S2 separately. For a display purpose, we removed the worst 1% channels in S1 for two rectification models *Rect(X)+Rec(Y)* and *Rect(X)+Rect(Y)+Rect(XY)*. (B) Comparison of each model's performance between S1 and S2 based on the cumulative probability distributions of the minimum difference. *, **, and *** indicates $p<0.05$, $p<0.01$, and $p<0.001$ due to Kolmogorov-Smirnov tests.

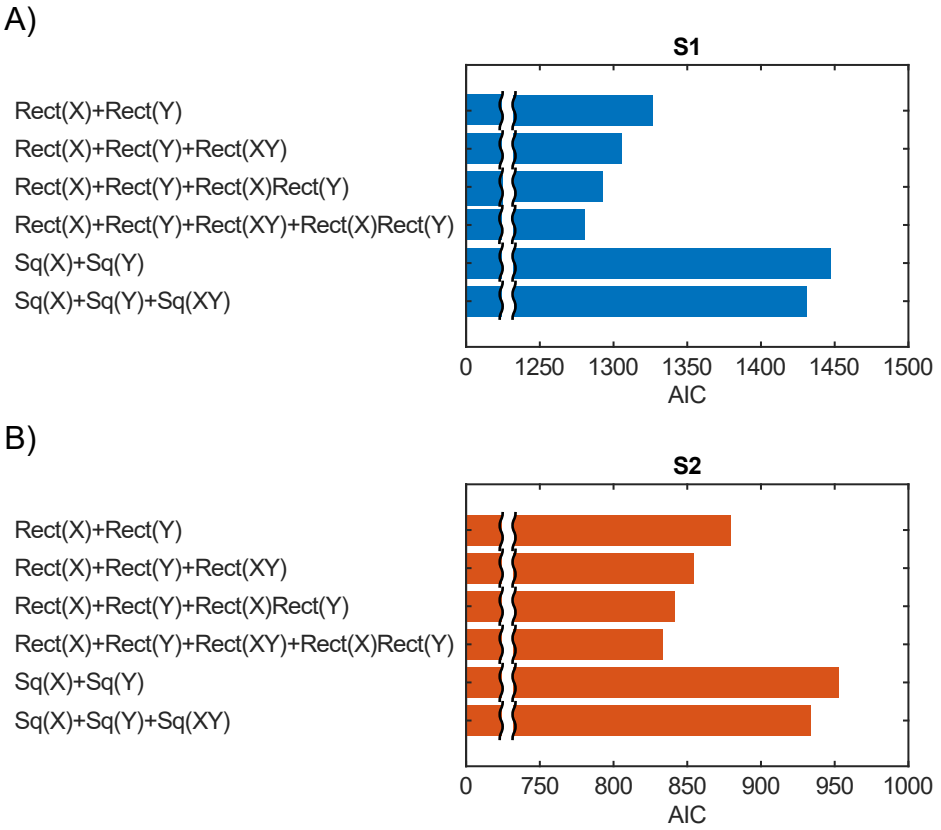

Fig 12. Akaike's Information Criterion (*AIC*) for 6 models for S1 and S2.

The best model is the full rectification model for both S1 and S2.

Supporting information

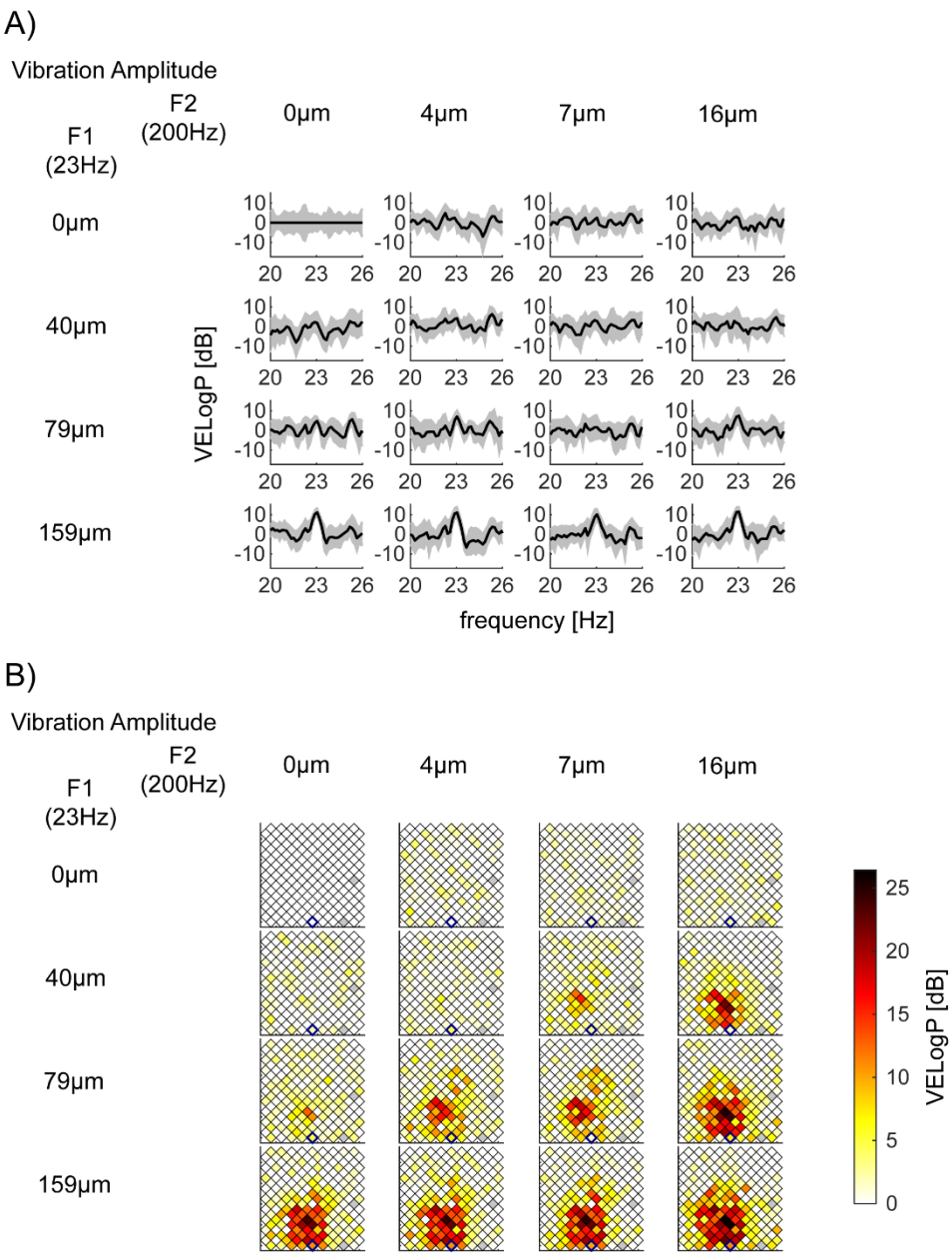

Sup Fig 1. Exemplar *VELogP* at *f1*=23Hz depend on the vibration amplitude of *F1*=23Hz. Shown with the same format as Fig 3. (A) *VELogP* of bipolar channel 176 in S1 (Session 2-2). This channel's responses at *f1*=23Hz showed a significant main effect of *F1*=23Hz amplitude only. *p*-value (*F1*, *F2*, interaction) = ($<10^{-5}$, 0.20, 0.042) with the corrected threshold 0.00016. (B) Spatial mapping of *VELogP* at *f1*=23Hz across all channels in S1 (Session 2-2).

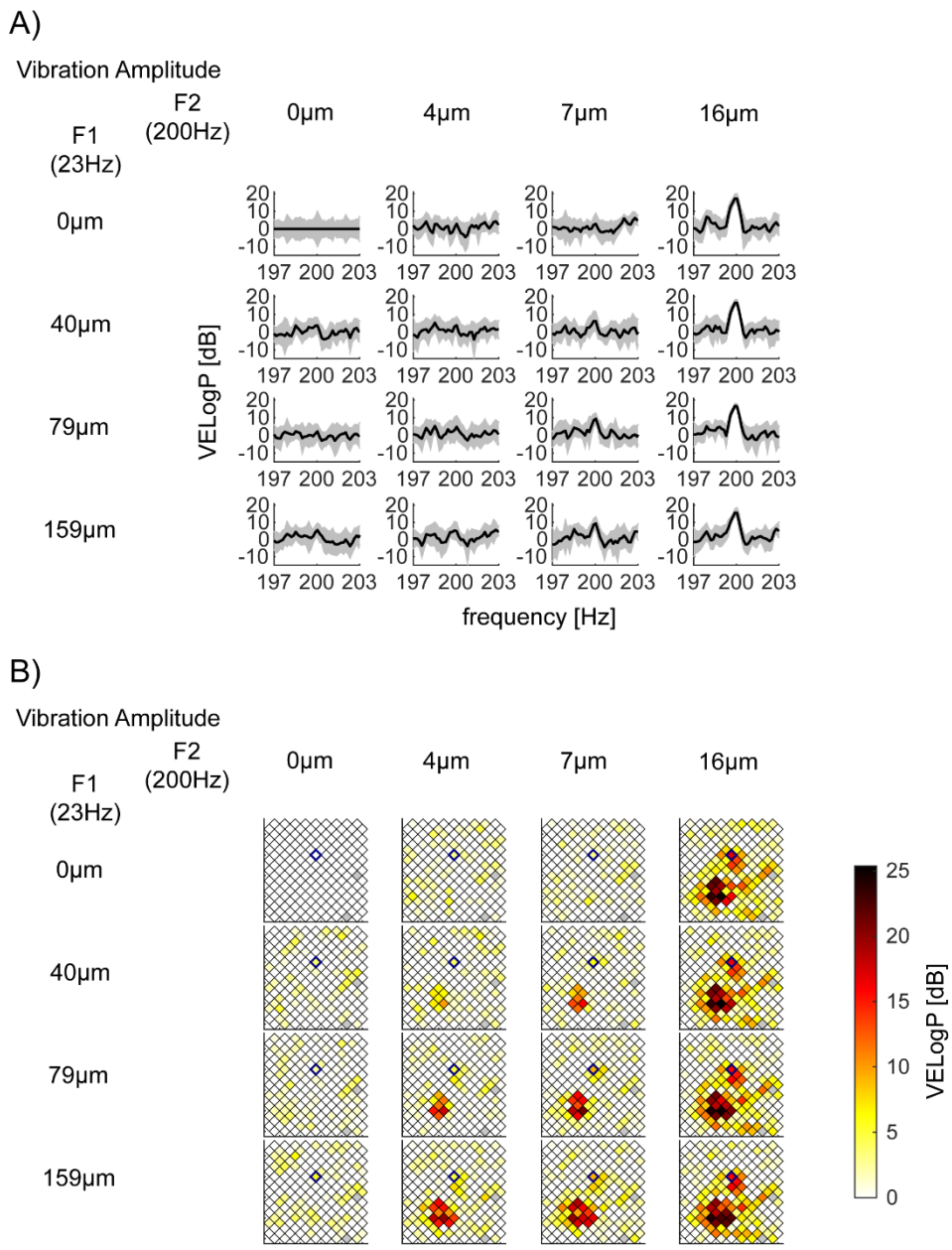

Sup Fig 2. Exemplar *VELogP* at *f2*=200Hz depend on the vibration amplitude of *F2*=200Hz. Shown with the same format as Fig 3. (A) *VELogP* of bipolar channel 122 in S1 (Session 2-2). This channel's responses at *f2*=200Hz showed a significant main effect of *F2*=200Hz amplitude only. *p*-value (*F1*, *F2*, interaction) = (0.0033, $<10^{-5}$, 0.045) with the corrected threshold 0.00016. (B) Spatial mapping of *VELogP* at *f2*=200Hz across all channels in S1 (Session 2-2).

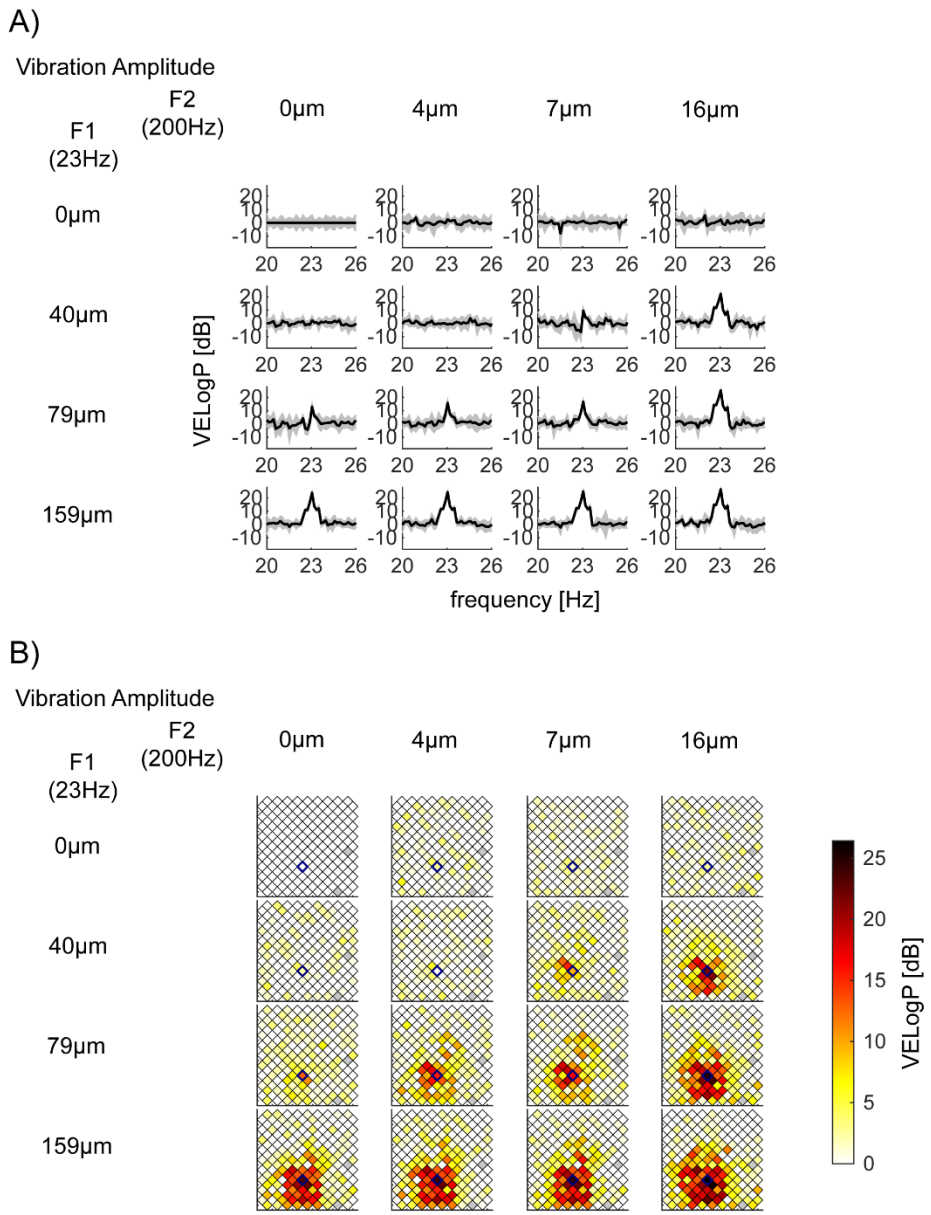

Sup Fig 3. Exemplar *VELogP* at *f1*=23Hz depend on the vibration amplitude of *F1*=23Hz, *F2*=200Hz, and their interaction.

Shown with the same format as Fig 3. (A) *VELogP* of channel 43 in S1 (Session 2-2). This channel's responses at *f1*=23Hz showed a significant main effect of *F1*=23Hz amplitude, the main effect of *F2*=200Hz, and their interaction. *p*-values (*F1*, *F2*, interaction) are all $p<10^{-5}$ with the corrected threshold 0.00016. (B) Spatial mapping of *VELogP* at *f1*=23Hz across all channels in S1 (Session 2-2).

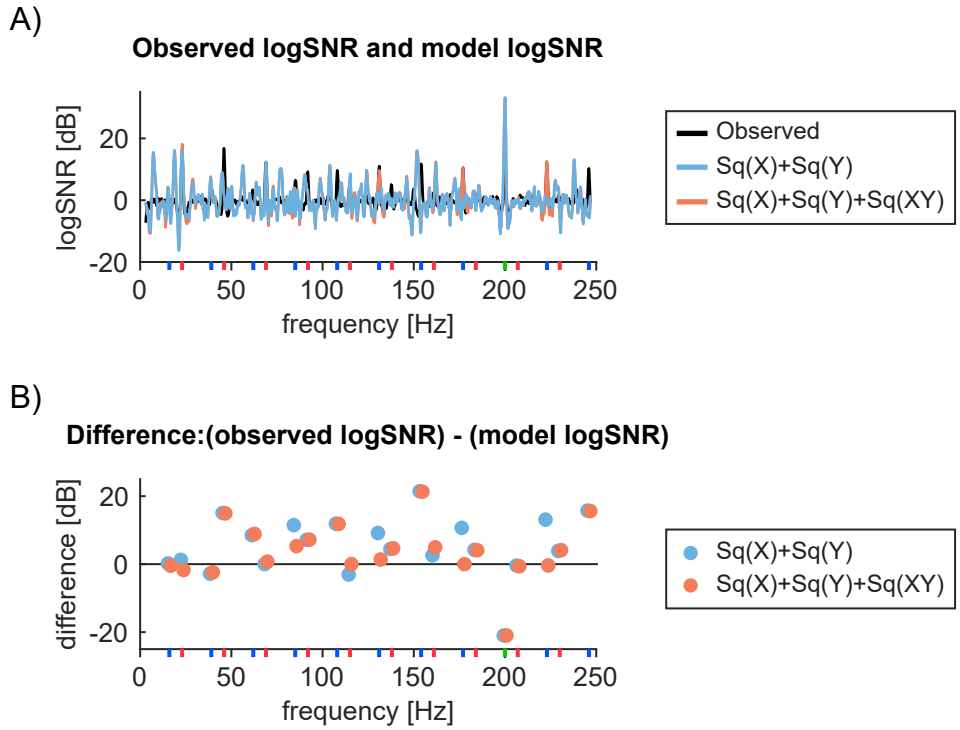

Sup Fig 4. Exemplar channel's observed and modelled responses for square wave models.

(A) Bipolar channel 43 in S1 (Session 2-2)'s log*SNR* (black) is compared to the optimally fitted models from two square wave models. The best parameters for each model are: (red) -0.82*Sq(X)*+56*Sq(Y)* and (blue) 1.0*Sq(X)*+83*Sq(Y)*+1.3*Sq(XY)*. The respective sums of log*SNR* differences from the observed log*SNR* across the frequencies of interest are 168 and 132. (B) Difference between the observed and the best model at the frequencies of interest. Color scheme is the same as in (A).

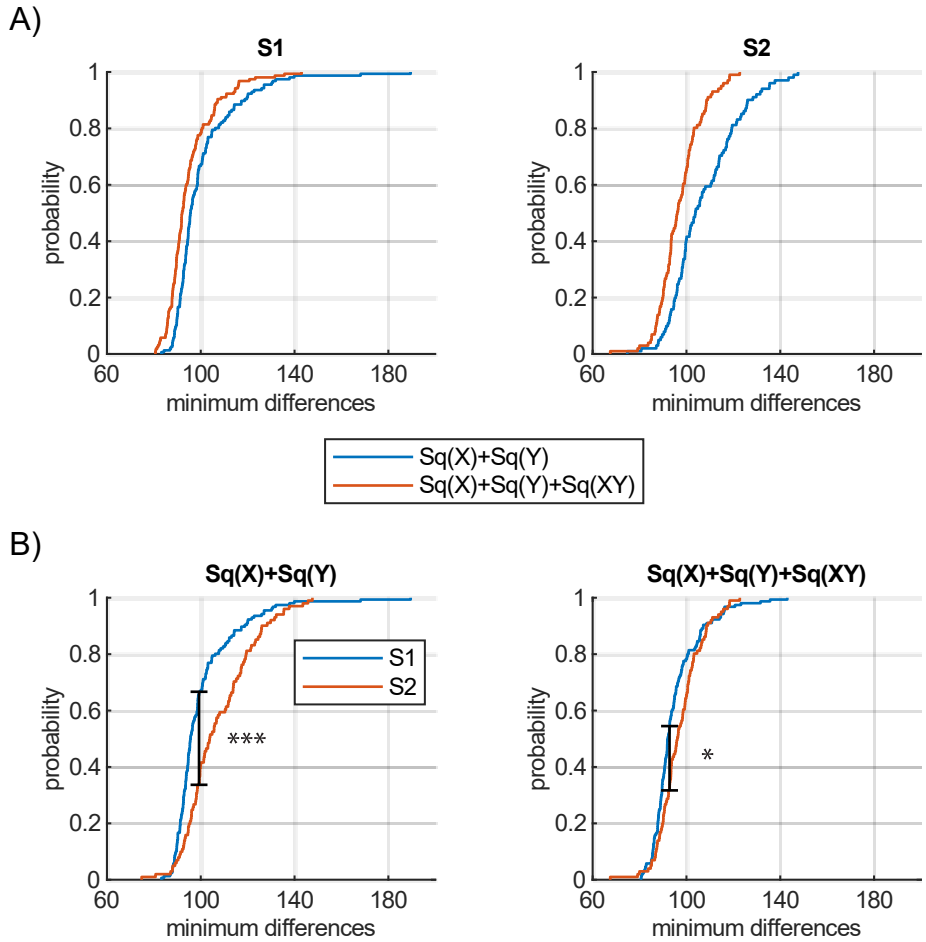

Sup Fig 5. Comparison of fitting performances across square wave models.

(A) Comparison of performance across two square wave models based on the cumulative probability distributions of the minimum difference for S1 and S2 separately. (B) Comparison of each model's performance between S1 and S2 based on the cumulative probability distributions of the minimum difference. * and *** indicates $p<0.05$ and $p<0.001$ due to Kolmogorov-Smirnov tests.

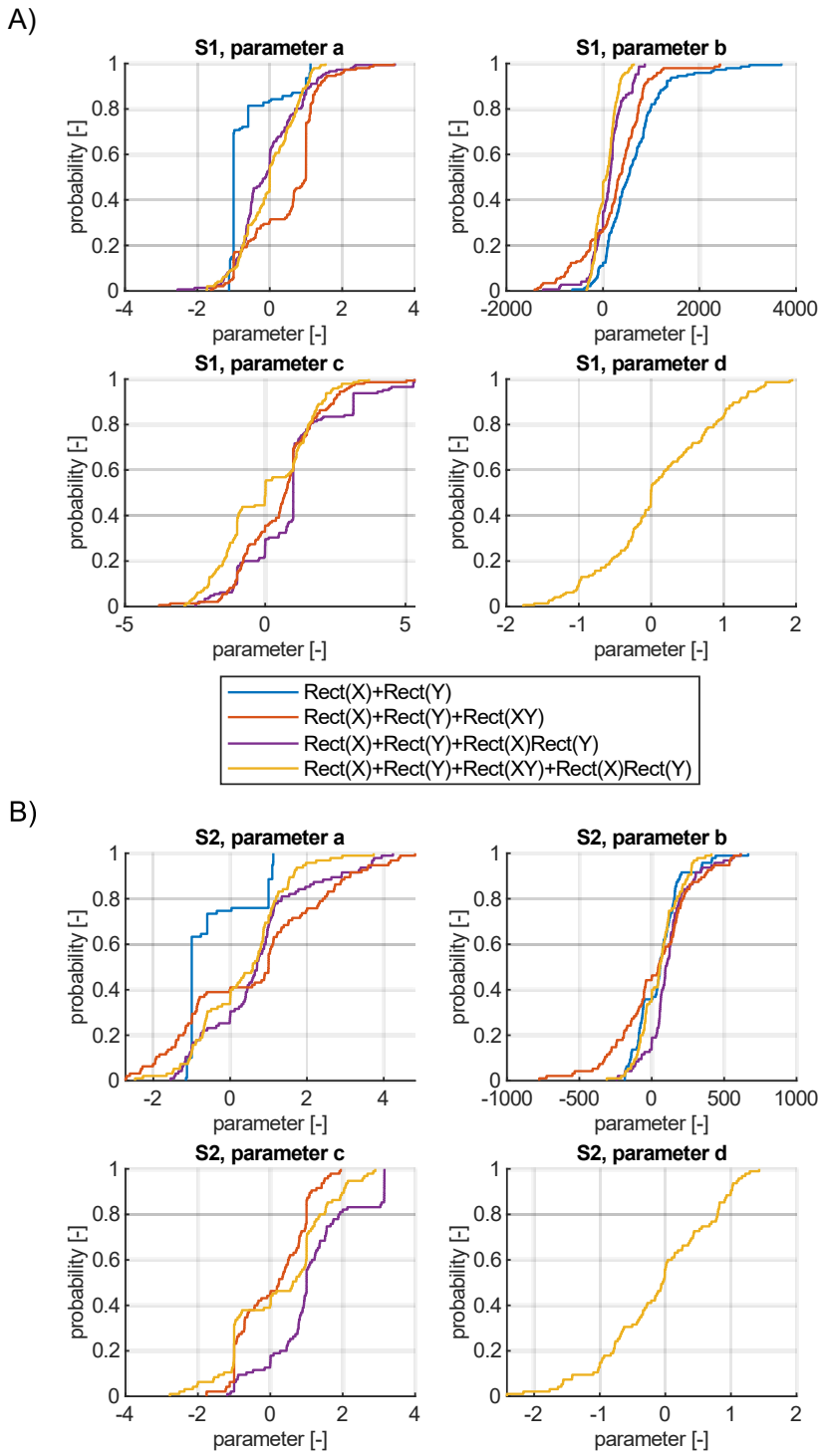

Sup Fig 6. Distribution of each coefficient in rectification models.

Cumulative probability distribution of each coefficient in S1 (A) and S2 (B). For a display purpose, we removed the top 3% and bottom 3% channels.

Sup Appendix 1. Line search optimisation technique.

For each model architecture, we used line search to find out a set of model parameters that minimized the difference between the model log*SNR* and the observed log*SNR*. (For the implementation of the following algorithm in MATLAB, see [1]).

We denote the difference that we tried to minimise as *d(i, p)* and define it as follows:

$$d(i,p) = \sum_{f \in F} \left| \log SNR^{p}_{model}(f) - \underline{\log SNR}^{i,[g_{\max},h_{\max}]}_{record}(f) \right| \quad (1)$$

d(i, p) is a function of channel *i* and a parameter *p* and it quantifies the sum of absolute differences of log*SNR* across a set of frequencies of our interest, *F. F* consists of fundamental (*f1* and *f2*), *f1* harmonic (46, 69, … up to 230), and intermodulation frequencies (16, 39, 62, 85, 108, 131, 154, 177, 223, 246). The underlined log*SNR* on the second term indicates the mean across trials for the stimulation condition with the maximum amplitude (i.e., g_{max} and h_{max}).

For line search, we used golden-section search [2]. This algorithm evaluates the objective function (i.e. *d(i, p)*) for four candidate parameters *p1, p2, p3,* and *p4*, where *p1, p2, p3, p4*∈*R* and *p1<p2<p3<p4*. If either *p2* or *p3* minimizes *d(i, p)*, the algorithm narrows down the search space by taking a new candidate within the search space. Otherwise, the algorithm expands the search space by taking a new candidate outside the search space. The golden-section search updates a candidate set of parameters (*p1, p2, p3, p4*) while keeping the same proportion, *r* : (1 - *r*), where *r* = *Φ* - 1 and *Φ* is the golden ratio.

Fig A1A demonstrates how the algorithm works. Here, in the first candidate set, *p2* minimizes *d(i, p)* which we denote as $p_{min_1} = p2$. The algorithm then set a new candidate parameter within *p1* and *p2* while keeping the golden ratio. The new candidate, *p5*, and the existing parameters (i.e. *p1, p2, p3*) constitute a new candidate set at the second step (the second row in Fig A1A, where $p_{min_2} = p3$). When the outermost value *p4* is selected at the *j*-th step, (e.g., $p_{min_j} = p4$ at the third row in Fig A1A), a new candidate parameter will be set at greater than *p4* while keeping the golden ratio.

The algorithm terminates when the improvement of the *d(i, p)* slows down from (*j*-1)-th step to the *j*-th step. Specifically, we terminate the algorithm when $d(i, p_{min_(j-1)}) - d(i, p_{min_j}) < ET$, where *ET* means error tolerance value, which we explain below. To avoid spurious termination, we also imposed another condition that (*p4 - p1)* < 0.0001, which ensures that our algorithm finds the minimum within a confined parameter range. If these criteria are satisfied at the *j*-th step, the algorithm returns the parameter giving the minimum *d(i, p)* in the *j*-th candidate set i.e. p_{min_j}.

When we considered a model architecture that had more than one coefficients, we sequentially optimized the coefficients in a fixed order. For example, for a model architecture with *aRect(X)+bRect(Y)*, we may first optimise coefficient *a* to be *a'* with the golden-section search. Then, we optimize *b* to be *b'* while keeping *a=a'*. We regard this sequential optimization of all coefficients as a single iteration of optimization (the orange lines and dots in Fig A1B), and we

iterated it 15 times. In the first iteration, we set initial candidate parameters as (*p1, p2, p3, p4*) = (-2, -2*r*, -2+2*r*, 0), (-1, 1-2*r*, -1+2*r*, 1), or (0, 2-2*r*, 2*r*, 2). In the *s*-th iteration when the previously optimised coefficient p_{s-1} from the (*s*-1)-th iteration is available, we started with (p_{s-1}, p_{s-1}+(1-*r*), p_{s-1}+*r*, p_{s-1}+1). While optimizing a parameter at the *s*-th iteration, we used the same error tolerance value *ET*(*s*). We set *ET*(*s*) to be 1 (for *s*=1….5), 0.1 (for *s*=6…10), and 0.01 (for *s*=11….15).

For any given channel *i* and a model architecture, we tried all possible combinations of initial parameter sets (3 possibilities) x all assignments of initial parameters (*N* possibilities for *N* parameters) x all orders of optimization (*N!* possibilities for *N* parameters) and reported the best across the combinations.

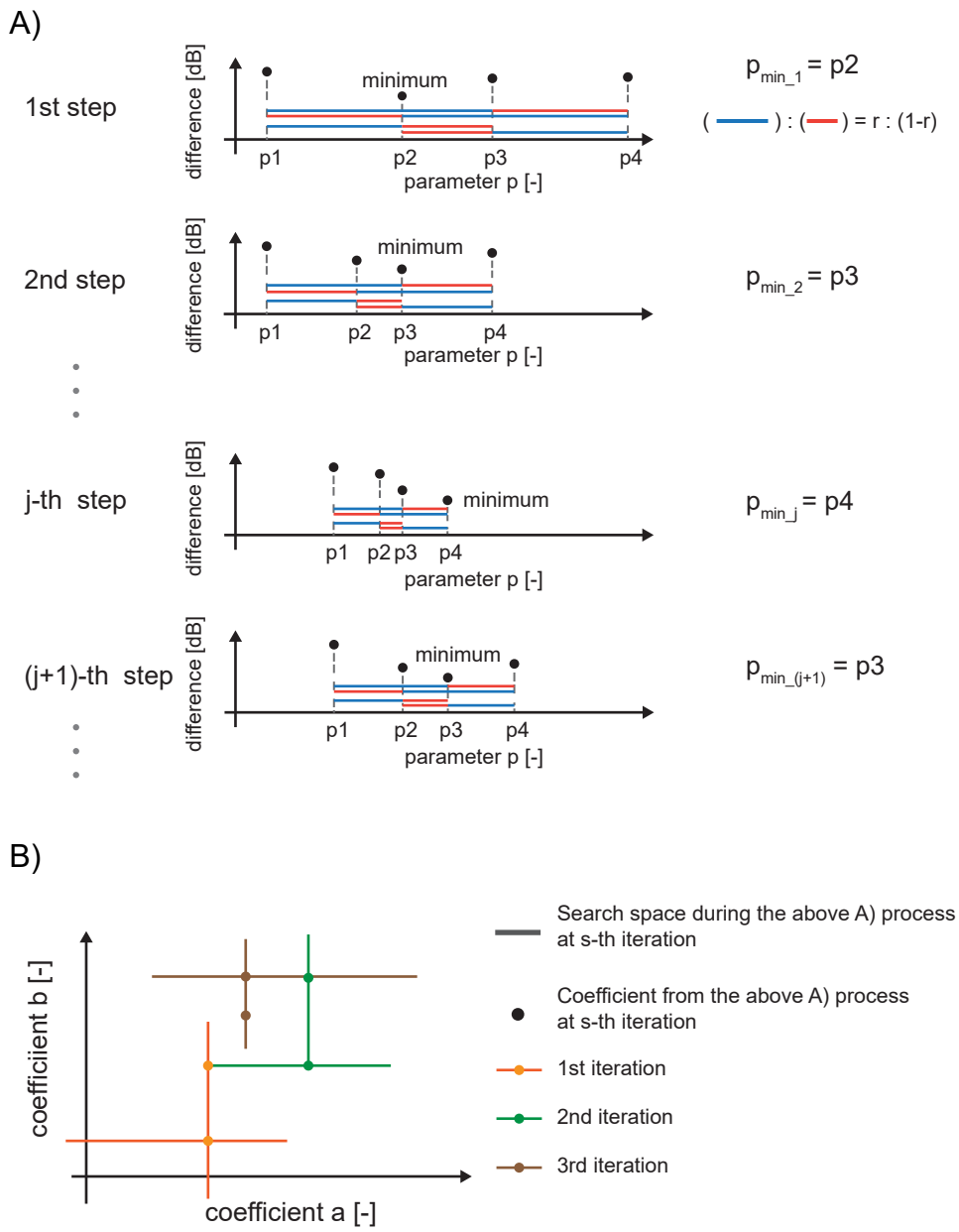

Fig A1. Explanation of Golden-section search algorithm.
(A) Single parameter optimization with Golden-section search. The algorithm takes four candidate points and computes their difference at each step. The point giving the minimum difference at the *j*-th step is shown as p_{min_j}. (B) Sequential optimization of two parameters. A line shows search space for each of single parameter optimization and a dot represents the optimized coefficient after the single parameter optimization depicted in A. This example optimised coefficient *a* first, then *b* at each iteration. Although we show up to the 3rd iteration here, we used 15 iterations to get results.

References

1. Kawshima Y, Li R. GitHub repository: yotaKawashima/mirror-tlab-unsw-catsomato. [cited 15 September 2020]. Available from: https://github.com/yotaKawashima/mirror-tlab-unsw-catsomato.git.
2. Scales LE. Introduction to non-linear optimization. New York: New York : Springer-Verlag; 1985.

Sup Appendix 2. Akaike's Information Criterion.

For model comparison, we computed Akaike's Information Criterion (*AIC*) [1]. *AIC* allows us to compare performances of models that differ in architecture (e.g., rectification vs. square wave) and in the number of parameters for each model. Specifically, we computed *AIC* for the least square model fitting with the following formula:

$$AIC = n\ln(\sigma^2) + 2K \tag{1}$$

, where n denotes the number of observations, σ^2 denotes the variance of the error term across the observations (in our case, n=156 for S1 and n=101 for S2, see the main text) considered for the model fitting, and K denotes the number of estimable parameters in a model, including the variance of the error term. The error term is the difference that we minimised by optimisation. Then, we computed the σ as the variance of the minimised difference across channels, assuming that the error term is normally distributed with mean = 0.

References

1. Burnham KP, Anderson DR. Multimodel Inference: Understanding AIC and BIC in Model Selection. Sociological Methods & Research. 2004;33(2):261-304. doi: 10.1177/0049124104268644.